Subsurface images of the Eastern Rift, Africa, from the joint inversion of body waves, surface waves and gravity: investigating the role of fluids in early-stage continental rifting

S. Roecker, C. Ebinger, Christel Tiberi, G. Mulibo, R. Ferdinand-Wambura, K. Mtelela, G. Kianji, A. Muzuka, Stephanie Gautier, Julie Albaric, et al.

Geophysical Journal International

Geophys. J. Int. (2017) **210,** 931–950
Advance Access publication 2017 May 19
GJI Geodynamics and tectonics

doi: 10.1093/gji/ggx220

Subsurface images of the Eastern Rift, Africa, from the joint inversion of body waves, surface waves and gravity: investigating the role of fluids in early-stage continental rifting

S. Roecker,[1] C. Ebinger,[2] C. Tiberi,[3] G. Mulibo,[4] R. Ferdinand-Wambura,[4] K. Mtelela,[4] G. Kianji,[5] A. Muzuka,[6] S. Gautier,[3] J. Albaric[7] and S. Peyrat[3]

[1] *Rensselaer, Troy, NY, USA. E-mail: roecks@rpi.edu*
[2] *University of Rochester, Rochester, NY, USA*
[3] *Géosciences Montpellier, CNRS-University of Montpellier, Montpellier, France*
[4] *University of Dar es Salaam Mlimani, Dar es Salaam, Tanzania*
[5] *University of Nairobi, Uhuru Highway, Nairobi* 00100*, Kenya*
[6] *Nelson Mandela Institute of Science and Technology, Kijenge, Arusha, Tanzania*
[7] *Chrono-environnement, University of Franche-Comte, Besançon, France*

Accepted 2017 May 18. Received 2017 April 7; in original form 2016 December 9

SUMMARY

The Eastern Rift System (ERS) of northern Tanzania and southern Kenya, where a cratonic lithosphere is in the early stages of rifting, offers an ideal venue for investigating the roles of magma and other fluids in such an environment. To illuminate these roles, we jointly invert arrival times of locally recorded *P* and *S* body waves, phase delays of ambient noise generated Rayleigh waves and Bouguer anomalies from gravity observations to generate a 3-D image of *P* and *S* wave speeds in the upper 25 km of the crust. While joint inversion of gravity and arrival times requires a relationship between density and wave speeds, the improvement in resolution obtained by the combination of these disparate data sets serves to further constrain models, and reduce uncertainties. The most significant features in the 3-D model are (1) *P* and *S* wave speeds that are 10–15 per cent lower beneath the rift zone than in the surrounding regions, (2) a relatively high wave speed tabular feature located along the western edge of the Natron and Manyara rifts, and (3) low (∼1.71) values of V_p/V_s throughout the upper crust, with the lowest ratios along the boundaries of the rift zones. The low *P* and *S* wave speeds at mid-crustal levels beneath the rift valley are an expected consequence of active volcanism, and the tabular, high-wave speed feature is interpreted to be an uplifted footwall at the western edge of the rift. Given the high levels of CO_2 outgassing observed at the surface along border fault zones, and the sensitivity of V_p/V_s to pore-fluid compressibility, we infer that the low V_p/V_s values in and around the rift zone are caused by the volcanic plumbing in the upper crust being suffused by a gaseous CO_2 froth on top of a deeper, crystalline mush. The repository for molten rock is likely located in the lower crust and upper mantle, where the V_p/V_s ratios are significantly higher.

Key words: Composition and structure of the continental crust; Africa; Joint inversion; Tomography; Crustal imaging; Continental tectonics: extensional.

1 INTRODUCTION

The role of magmatism in the early stages of cratonic continental rift zones remains a subject of debate. The vertically integrated strength of cold, thick, cratonic lithosphere is greater than the far-field, gravitational potential energy and dynamic mantle traction forces available, suggesting that additional forces are required to initiate rifting (e.g. Bott 1990; Stamps *et al.* 2014). Where rifting initiates near or above an upwelling and anomalously hot mantle, melt may be generated in the uppermost mantle, and buoyantly intrude the thick, cold cratonic lithosphere. The dike and sill intrusions transfer heat, and may serve to localize further injections, effectively reducing the integrated strength and facilitating rift initiation (e.g. Buck 2004; Bialas *et al.* 2010). Volatiles may also transfer from the mantle to the lithosphere, and hydrate the mantle rocks, leading to widespread metasomatism and mantle strength reduction (e.g. Mackwell 1998; Maggi *et al.* 2000).

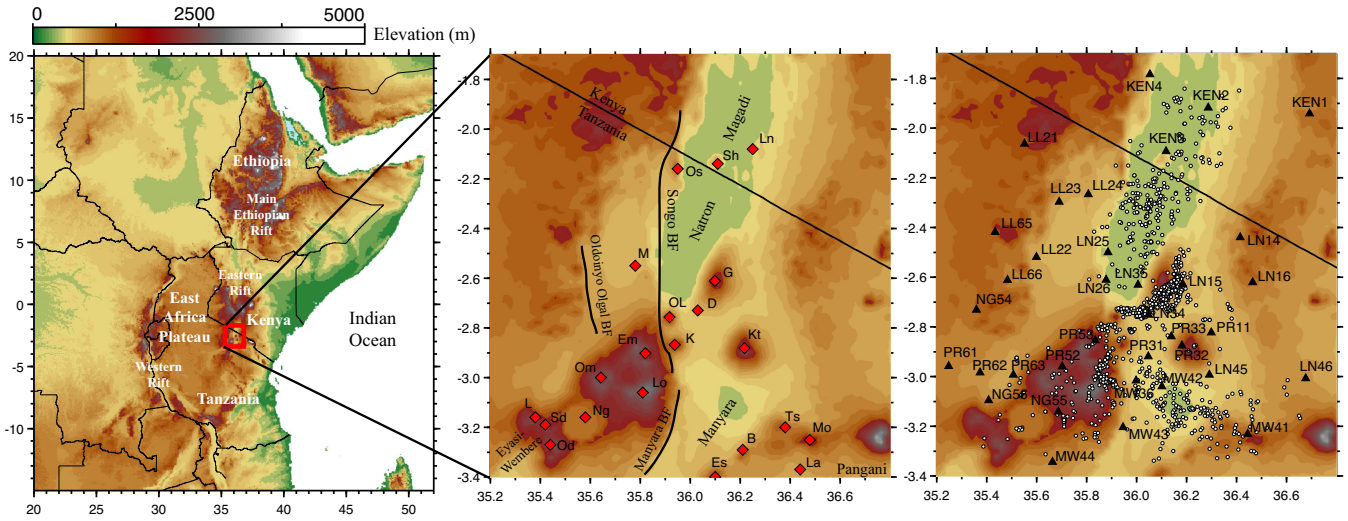

Figure 1. Left: location of the Eastern Rift System (ERS) in the context of the East Africa Rift Zone. Red rectangle locates the area of investigation. Centre: locations of major basins, bounding faults and recent eruptive centres in the area of investigation. Eruptive centres are indicated by solid red diamonds and identified with initials as follows: B, Burko; D, Dike Swarms; Em, Embagai; Es, Essimingor; G, Gelai; K, Kerimasi; Kt, Ketumbeine; L, Lemagrut; La, Lashaine; Ln, Lenderut; Lo, Loolmalasin; M, Mosonik; Mo, Monduli; Mu, Meru; Ng, Ngorongoro; Od, Oldeani; OL, Oldoinyo Lengai; Om, Olmoti; Os, Oldoinyo Sambu; Sd, Sadiman; Sh, Shompole; Ts, Tarosero. BF stands for Boundary Fault. Right: Broad-band seismic stations of the CRAFTI-CoLiBrEA network are indicated by solid black triangles with station codes. Epicentres of local events recorded during the deployment are shown by solid white circles.

With several rift segments at different stages of the rifting cycle, and the last orogenic episode more than 500 Mya, the young (<7 My) Eastern Rift System (ERS) in northern Tanzania and southern Kenya (Fig. 1) offers an ideal venue to study the role of magma and other fluids in the early stages of rifting in cratonic lithosphere. This area is associated with a change both in the structural expression of the rift (Dawson 1992; Foster *et al*. 1997; Le Gall *et al*. 2008) and in magmatic behaviour (Nonnotte *et al*. 2008; Mana *et al*. 2015; Lee *et al*. 2016). The southern sector of the ERS developed along the eastern margin of the deeply-rooted Archaean Tanzania craton (e.g. Ritsema *et al*. 1999; Weeraratne *et al*. 2004), and it encompasses the active carbonatitic volcano, Oldoinyo Lengai (e.g. Dawson *et al*. 1994; Fischer *et al*. 2009). The Magadi–Natron–Manyara basin system (Fig. 1) is also one of the most seismically active East African rift sectors, with abundant lower crustal earthquakes (e.g. Mulibo & Nyblade 2009; Albaric *et al*. 2010; Yang & Chen 2010; Weinstein *et al*. 2016).

In this study, we focus on the manifestations of magmatic activity in the crust of the ERS to shed some light on how magma migrates from repositories in the lower crust/upper mantle to the surface. We do so through a joint analysis of locally recorded *P*- and *S*-wave arrival times, ambient noise generated Rayleigh waves, and gravity observations. By jointly inverting these data sets, we generate a 3-D image of the upper 25 km of the subsurface at significantly higher resolution and consistency than would have been possible by treating them separately. We find evidence that the volcanic plumbing in the upper crust is suffused by a gaseous CO_2 froth on top of a deeper, crystalline mush, and that the repository for molten rock is likely located in the lower crust and upper mantle. Our results indicate extensive modification of crustal structure by magmatism and stretching during the very early stages of continental rifting.

2 TECTONIC FRAMEWORK

The ERS extends from southern Ethiopia to central Tanzania, and marks the divergent plate boundary between Nubia and Somalia (e.g. Saria *et al*. 2013; Fig. 1). Uniquely, the surface expression of the Eastern rift fractures the deeply-keeled Archaean Tanzania craton; topography at the base of the craton influenced the location and development of magmatism and rift extension (e.g. Ebinger & Sleep 1998; Weeraratne *et al*. 2003; Vauchez *et al*. 2005). Inverse and forward models of gravity and topography indicate that the Tanzania craton is underlain by strong lithosphere, with weaker lithosphere beneath a slightly stretched rift (Petit & Ebinger 2000; Pérez-Gussinyé *et al*. 2009). Rifting initiated at ∼25 Ma in the northern sector of the ERS, whereas the southern sector of the ERS developed after ∼6 Ma, based on Ar–Ar dating of volcanic samples, and abundant faunal remains in the Olduvai-Natron basins (e.g. Ashley 2007; Mana *et al*. 2012, 2015). In northern Tanzania, the Natron–Manyara rift zone of the ERS splits into three distinct segments: the Eyasi–Wembere rift, the Manyara rift, and the Pangani rift. The Manyara border fault displaces originally flat-lying basalts, trachytes, and sediments of *ca.* 1 My age, indicating that basin subsidence and rift flank uplift occurred during the past 1 My.

Controlled-source and passive seismic, gravity, structural, geodetic, magnetotelluric, petrological and xenolith studies provide a strong regional framework in which to interpret short- and long-term strain patterns (e.g. Henjes-Kunst & Altherr 1992; Rudnick *et al*. 1993; Mechie *et al*. 1994; Birt *et al*. 1997; Foster *et al*. 1997; Simpson *et al*. 1997; Chesley *et al*. 1999; Calais *et al*. 2008; Albaric *et al*. 2010; Saria *et al*. 2013; Tarits *et al*. 2014). Local shear wave, surface wave and SKS-splitting measurements along the ERS show a rift-parallel anisotropy that is primarily caused by aligned melt zones in the lithosphere, whereas patterns outside the rift are affected by the cratonic keel (e.g. Walker *et al*. 2004; Weeraratne *et al*. 2004; Kendall *et al*. 2006; Albaric *et al*. 2014). Geochemistry and petrology of mantle xenoliths indicate that the base of the lithosphere beneath the Archean craton (west), the rift, and Pan-African belt (east) have been affected by the impingement of a mantle plume and extensive mantle metasomatism (Chesley *et al*. 1999; Fischer *et al*. 2009; Baptiste *et al*. 2015). Crustal xenoliths from Archaean crust and Pan-African crust are Archaean age mafic granulites (Jones *et al*. 1983; Mansur *et al*. 2014), suggesting

similar lower crustal compositions on either side of the Archaean-Pan-African suture. Heat flow data show little to no elevation of geotherms beneath the 1.5–2 km rift flanks and low heat flow across the Archaean craton. Heat flow is high but spatially variable within the rift valley, indicating advective transfer by magmatism and hydrothermal fluids (Nyblade *et al*. 1990; Wheildon *et al*. 1994).

In the southern sector of the ERS, seismicity rates are high, with some of the deepest continental rift events (Nyblade *et al*. 1996; Foster & Jackson 1998; Albaric *et al*. 2010; Yang & Chen 2010), yet eruptive centres are also present (Fig. 1). Transmission is efficient, with M_L 3 events recorded at distances greater than 500 km (Langston *et al*. 1998; Weinstein *et al*. 2016). Faults are unusually long (20–120 km) and widely spaced (10–20 km), enabling correlations of seismicity with individual fault traces (e.g. Foster *et al*. 1997). Models of InSAR data show that 40 per cent of the volcanoes in the Kenyan section of the ERS rift (north of our study area) inflated and/or deflated between 1997–2008, indicating additions and removal of magma, gas, and/or water interactions (Biggs *et al*. 2009). None of these magmatic events were accompanied by eruptions, implying that the eruption record is not a good proxy for magmatic events, which are relatively common. The Natron basin region was the site of faulting, magma intrusion, and a volcanic eruption in 2007–2008 (e.g. Baer *et al*. 2008; Calais *et al*. 2008; Biggs *et al*. 2013). The Natron crisis provides compelling evidence for strain accommodation by magma intrusion in addition to slip along large-offset normal faults during the early stages of continental rifting. The Eastern rift system in southern Kenya and northern Tanzania thus offers several advantages for studies of strain partitioning via magmatism and faulting over both the rifting cycle time scale (100 s of years) and as the rift zone evolves over several millions of years.

3 DATA AND PRE-PROCESSING

3.1 Seismic data

The seismic data analysed in this study include a combination of arrival times from local earthquake-generated body waves and phase delays from ambient noise generated surface waves recorded by seismic stations deployed in the ERS (Fig. 1). Most of these data were recorded by the joint Continental Rifting in Africa: Fluid/Tectonic Interaction (CRAFTI) and Continental Lithospheric Breakup in East Africa (CoLiBrEA) networks of 36 total broad-band stations, supplemented by two permanent stations (KIBK and KMBO) from the GEOFON Global Seismic Network.

The CRAFTI- CoLiBrEA network operated in the northern Tanzania ERS from January 2013 to December 2014 and included a combination of STS-2, CMG-3T, CMG-40T and Trillium sensors. Data collected during most of 2013 were plagued by massive failures of the GPS clocks due to unknown (but most likely environmentally related) causes. These clocks were replaced in late 2013 with a clock model that seemed to be immune to these effects. Green's functions generated from ambient noise cross-correlations show that relative drift rates of these unlocked clocks were substantial and erratic (Fig. 2). While some information about timing might be determined with corrections derived from such analysis, for purposes of this study, we use only data recorded when reliable GPS timing was available (2013 January 18–February 12, and 2013 December 1–2014 December 1).

3.1.1 Body waves from local earthquakes

The initial body wave data set was derived from a subset of a CRAFTI-CoLiBrEA database of 3427 earthquakes (Weinstein *et al*. 2016), and consists of 29 958 *P* and 33 521 *S* arrival times from the 2528 events that were well recorded and located within the tomographic model volume. These arrival times and their associated uncertainties are estimated manually after band-pass filtering the waveforms between 1and 12 Hz. Nominal uncertainties for *P*-wave arrival times are between 0.1and 0.3 s while those for *S*-waves typically are about twice that amount. During each iteration for a new model, we relocate hypocentres and retain those that are located within the model boundaries and are recorded by at least 10 stations with predicted arrival times that have residuals less than the larger of 0.5 s and 5 per cent of the total travel time. While this is a dynamic selection process (observations classified as potential outliers in one

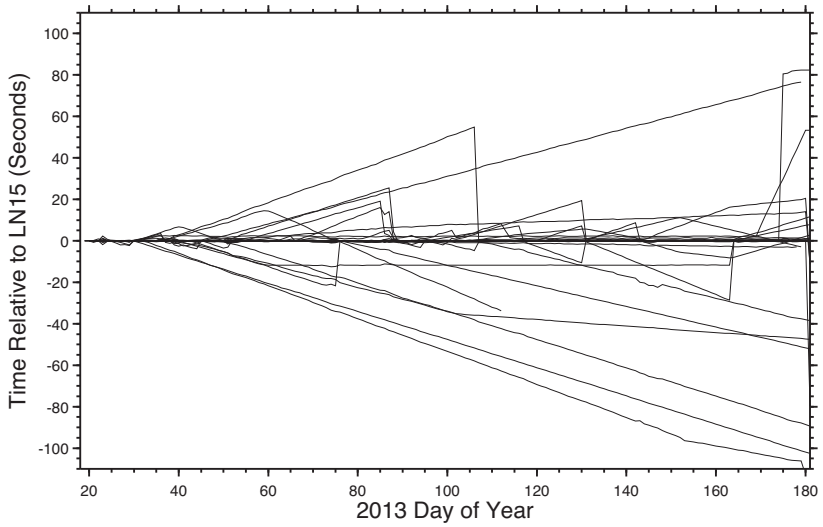

Figure 2. Clock drift of the RefTek RT130s in the CRAFTI-CoLiBrEA network resulting from the failure of GPS clocks during the first half of 2013, determined by cross-correlating day volumes of ambient noise Green's functions using a technique similar to that described by Sens-Schönfelder (2008). Times are relative to the clock at station LN15, one of the few that remained in operation during that time. Note the large amount of drift and occasional erratic behaviour of the clocks, which discouraged analysis of data from this time period.

iteration can be reconsidered in subsequent iterations), application of these criteria typically results in a data set of about 1500 events, with a variation of about 10 events between iterations, comprising approximately 17 000 *P* and 20 000 *S* arrival times. We note that the iterative inversion is convergent, with subsequent iterations experiencing gradually smaller perturbations and reduction in residual variance. This shows that the dynamic selection procedure is stable and not dependent on the inclusion or exception of a small subset of observations.

3.1.2 Rayleigh waves from ambient noise data

The 38 broad-band stations (36 from CRAFTI-CoLiBrEA, 2 from GEOFON) provide 583 contemporaneous station pairs, from which Green's functions may be estimated. The steps used in generating surface wave phase delay times from the ambient noise are similar to those described in Comte *et al*. (2016). We summarize those steps here, emphasizing how our application differs from theirs.

We followed the pre-processing steps described by Bensen *et al*. (2007) to generate estimated Green's functions (EGFs) from the vertical component of cross-correlated noise, using a version of the CU-Boulder ANCC software,[1] modified to permit sampling and frequency bands appropriate for our data. Running-mean normalization was used to reduce contamination by coherent signals (mostly from earthquakes), and we pre-processed periods between 2 and 150 s.

Cross-correlations for each contemporary station-pair were generated for each day of record, and were then stacked over the duration of co-recording. In an attempt to improve the signal-to-noise ratio (SNR) of the final stack, we iteratively removed daily correlations that deviated by more than one standard deviation from the overall stack. In contrast to Comte *et al*. (2016), we found that the SNR of the iteratively refined stack improved on average by a factor of two from those obtained from a simple stack of the entire data set.

We measured phase velocity dispersion using a technique based on that described by Yao *et al*. (2006). The EGFs are narrow-band filtered at 1 s intervals between 4 and 30 s in a passband of ± 0.2 s of the central period and are windowed within three cycles of an estimated arrival time. Noise is sampled in a part of the seismogram before the expected arrival, and seismograms with an SNR less than a given threshold (usually 10) are excluded. Those remaining are transformed to a velocity versus period space and a phase velocity dispersion curve is determined by tracking amplitude maxima over available periods. In practice, simply following the maxima does not guarantee immunity from cycle skips, and hence as a pre-processing step, we generated a pilot dispersion curve from a least squares fit to all of the original curves that appear to fall within the correct cycle. In this case, the pilot curve for phase velocity c (in km s^{-1}) as a function of period T (in seconds) was represented by the polynomial

$$c(T) = 2.995304 + 0.040571T - 0.000361T^2. \quad (1)$$

For each EGF, we choose the cycles that most closely follow this curve. Points without a clear maximum near the pilot curve were visually re-examined and discarded if ambiguous. Examination of dispersion curves from several station pairs suggested that cycle skips could be reliably identified at periods longer than 5 s; hence, we adopt that as a minimum period. We also found that these curves tended to diverge at periods corresponding to the three-wavelength rule of Bensen *et al*. (2007), and so we used that rule to enforce a long-period cut-off. For the aperture of this network, the three-wavelength rule translates to a maximum period of about 14 s.

Because of the proximity of the stations to the Indian Ocean (Fig. 1), one may be concerned that an azimuthally inhomogeneous distribution of noise could significantly bias the phase velocities determined from the EGFs. This concern was reinforced by both the asymmetry of some of the EGFs and discrepancies in dispersion curves generated by the causal and acausal sides of some of the cross correlations.

To estimate and correct for this bias, we employed a technique based on that described by Yao & van der Hilst (2009), with modifications described by Comte *et al*. (2016), to estimate the azimuthal distribution of noise $E(\theta)$ for each period of interest (Fig. 3). We then use these noise estimates to calculate a phase shift, $\delta\phi_n$, at radial frequency ω between an observed cross-correlation and one that would have resulted from an isotropic distribution of noise (i.e. $E(\theta) = 1$). The bias μ is defined by

$$\mu = -\frac{\delta\phi_n}{\omega t_n} = \frac{t_n^{\mathrm{iso}} - t_n}{t_n} \quad (2)$$

where t_n is an estimate of the phase-delay time between station-pair n derived from a 2-D phase velocity map using dispersion curves generated from averaged cross correlations (causal and acausal). The estimates of the 'true' phase delay time, t^{iso}, are then used to update the phase velocity maps. This process may be iterated until the estimates of t^{iso} stabilize. For the data set used here, stability was achieved after a single iteration.

Surprisingly, the noise distribution we determined (Fig. 3) is dominated by sources located SSW of the network, which roughly corresponds to the strike of the rift valley. This suggests that even though one would expect the major source of noise to be from the Indian Ocean to the ESE, the low wave speeds in the rift valley appear to act as a waveguide for noise from the north and south. The biases resulting from this noise distribution are generally small but could be as large as 1.5 ± 0.15 per cent (Fig. 4). Note that the variation in the maximum bias for different periods is a function of the amplitude of $E(\theta)$ at that period. These estimated biases were used to adjust the surface wave phase delay times and new phase velocity maps (Fig. 5) were computed. The phase delay times derived from these maps are then used in the joint inversion with the body wave arrival times. We note that because the bias is generally much smaller than the variation in phase velocity ($\sim\pm 10$ per cent) the revised phase velocity maps look very similar to the original ones.

Estimates of uncertainties in surface wave phase delay times are based on the SNR of the EGF used in generating the dispersion curve, multiplied by a factor related to the period (longer periods generally have less well defined maxima). The average uncertainty is about 0.5 s. Outliers in the surface wave data set are identified and removed during the creation of phase velocity maps as part of the noise bias analysis.

3.2 Gravity data

The gravity observations used in our study are taken from the point database compiled by Ebinger *et al*. (1997) and Tesha *et al*. (1997), along with ~200 new gravity stations occupied during this project (Tiberi *et al*. 2016; Supporting Information Fig. S1). Gravity stations are spaced between 2–20 km within the rift valleys and the flanks, with gaps as large as 50 km at the western edge of the grid. The rift gravity field is superposed on a long wavelength anomaly associated with dynamic compensation for the East African plateau.

[1] Available at: http://ciei.colorado.edu/Products/

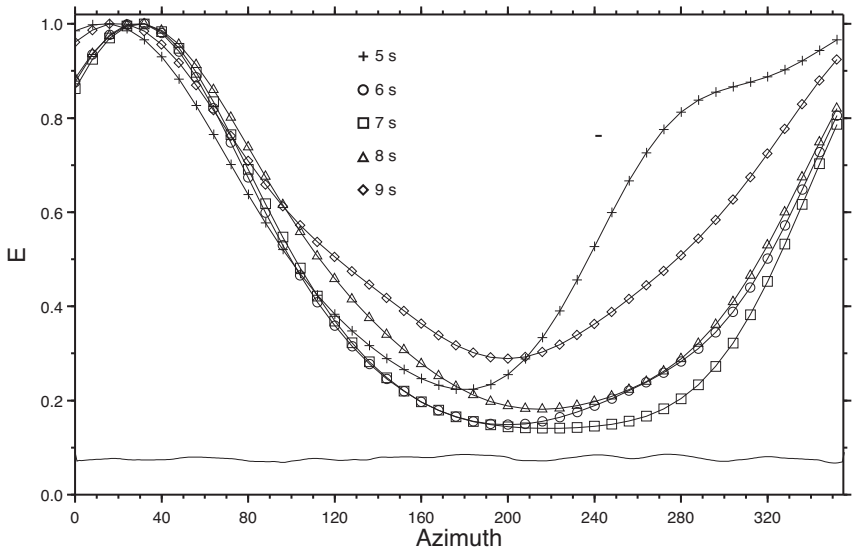

Figure 3. Normalized noise energy E as a function of propagation azimuth (θ) for periods between 5 and 9 s. Maximum 2σ uncertainties are $\sim\pm 9$ per cent for the periods analysed and are shown as a function of azimuth by the solid line near the bottom of the figure. Note that the peak in this period range is at about 30 °, meaning that most of the noise recorded by the CRAFTI-CoLiBrEA network propagates along the rift valley from SSW to NNE.

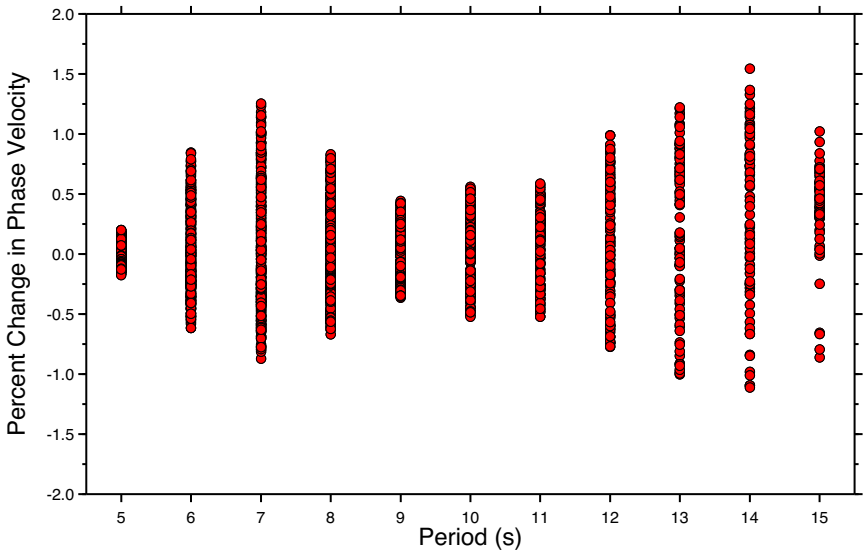

Figure 4. Biases in phase velocities caused by the inhomogeneous azimuthal distribution of noise as a function of period. Uncertainties in these biases are on average about 10 per cent of the value, so for example a 1 per cent change in phase velocity has an associated uncertainty of ± 0.1 per cent. Revised phase delay times are derived from phase velocity maps corrected for these biases.

We use a transfer function between gravity and topography (Ebinger *et al*. 1989) to filter the long-wavelength topography associated with sublithospheric density anomalies. Gravity uncertainties are difficult to assess quantitatively, and combine both an observational and theoretical error (from the uncertainties in the predictions of the $\rho(V_p, V_s)$ transfer function). We estimate the average uncertainty to be about 1 mgal.

4 JOINT INVERSION METHODOLOGY

Like most joint inversions, the simultaneous fitting of disparate data sets is motivated by complementary sensitivities of these observations to different parts of the model. For example, while we have many more body wave observations, surface wave and gravity data improve sampling in parts of the model where there are few (or no) body wave ray paths. The surface waves also help to compensate for the higher uncertainties in the shear wave arrival times.

The method for joint inversion of local earthquake body wave travel times and ambient noise surface wave dispersion curves is similar to that described by Comte *et al*. (2016), which in turn is based on an approach described by Nunn *et al*. (2014) modified for the local event case using procedures described by Roecker *et al.* (2004, 2006). The inclusion of gravity data is adapted from an approach described by Roecker *et al*. (2006), modified for spherical coordinate systems by Li *et al*. (2011).

4.1 Forward problems

The model space is parameterized by specifying *P* and *S* wave speeds on a 3-D grid of nodes, spaced 0.02 ° (~2 km) in latitude and

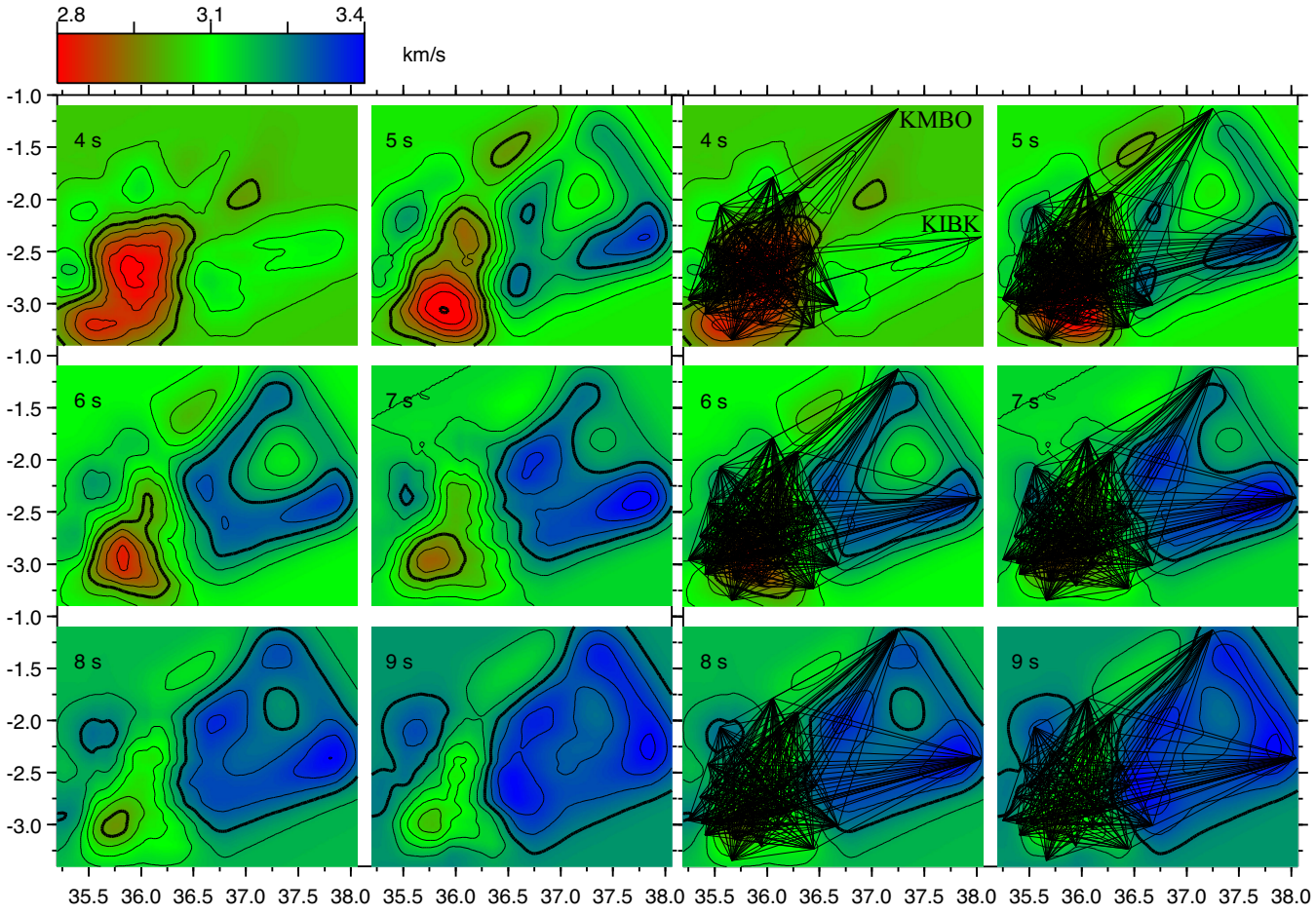

Figure 5. Left two columns show examples of phase velocity maps for periods of 4 to 9 s. Thin contour interval is 0.05 km s^{-1}; thick interval is 0.25 km s^{-1}. Right two columns show the same maps with the ray paths used at each period plotted on top of the maps. Paths to the NE corner are to the GEOFON stations KIBK and KMBO in Kenya. For the joint inversion, we use only those parts of the paths that are west of 36.8 °E and south of 1.7 °S.

longitude and 1 km in depth. Intra-grid wave speeds are determined by trilinear interpolation. Body wave travel times within the medium are calculated using a 3-D eikonal equation solver in a spherical (Earth-centred) coordinate system (Li *et al*. 2009; Zhang *et al*. 2012). Surface wave phase delay times at a given frequency ω and a given 3-D V_s model are determined by first assuming that such a model can be constructed by combining 1-D models at each areal grid point (Montagner 1986). With this assumption, we calculate phase velocities c and partial derivatives $\partial c/\partial V_s$ for the 1-D model at each areal point using the locked-mode method of Gomberg & Masters (1988). The phase delay time between any two points is then calculated by integrating the reciprocal of the phase velocity along the great circle path between them.

The gravity forward problem is solved by using the same 3-D grid of nodes and assuming a constant density within a spherical element centred at each node. The gravitational attraction of a single spherical element is calculated using the recursive method of Li *et al*. (2011), based on the elementary source technique of Asgharzdeh *et al*. (2007). Following the procedure of Roecker *et al*. (2006), we couple the gravity and arrival time inversions by specifying a general relationship between density and wave speeds. As we have few constraints on such relationships for our study area, we start with the $\rho(V_p)$ function suggested by eq. (1) of Brocher (2005) for a wide variety of rock types. We can use this relationship to derive an equivalent single-valued $V_p(\rho)$ function, and extend it to include an explicit dependence of V_s on V_p (i.e. $\rho(V_p, V_s(V_p))$) using the $V_s(V_p)$ relation in eq. (6) of Brocher (2005). However, this assumes a dependence on Poisson's ratio that is likely not appropriate for our area. An alternative would be to substitute a $V_s(V_p)$ function from the wave speeds determined by the joint body wave/surface wave (JBS) model (discussed below), which should be better suited to our area. A best fit cubic polynomial that serves this purpose (Fig. 6) is

$$V_s \text{ (km s}^{-1}) = 3.1632 + 0.6081\hat{V}_p - 0.0269\hat{V}_p^2 - 0.0059\hat{V}_p^3, \quad (3)$$

where $\hat{V}_p = V_p - 5.4111$ km s^{-1}. While this is an improvement, the resulting $\rho(V_p, V_s(V_p))$ function suffers from restricting, and potentially overly biasing against, the variability in Poisson's ratio already evident in the JBS model for different values of V_p or V_s. We relax this restriction by posing $\rho(V_p, V_s)$ as a transfer function, defined as a ratio of polynomials

$$\rho(V_p, V_s) = \frac{\sum_{i=0}^{n}\sum_{j=0}^{i} c_k V_p^{i-j} V_s^j}{\sum_{i=0}^{q}\sum_{j=0}^{i} d_k V_p^{i-j} V_s^j} \quad (4)$$

where the subscript $k = i(i+1)/2 + j$. We require the transfer function to be consistent with the $\rho(V_p, V_s(V_p))$ relation derived from $\rho(V_p)$ relation of Brocher (2005) and the $V_s(V_p)$ function determined from the traveltime inversion. Hence, we estimate values for the coefficients c_k and d_k by least squares minimization of the difference, calculated over a range of densities (ρ = 2.0–3.4 g cm^{-3}),

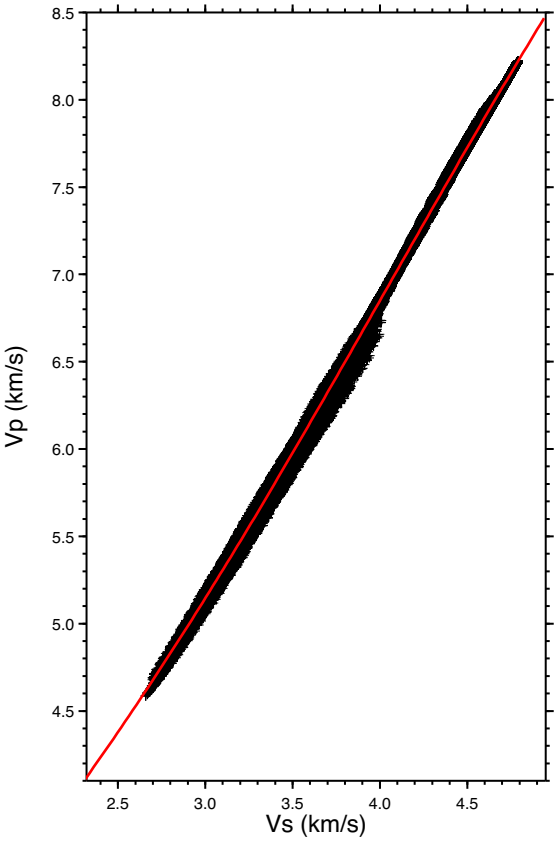

Figure 6. Plot of V_p versus V_s for the JBS model. The red line is the cubic polynomial in eq. (3) used in generating the density transfer function in eq. (4).

Table 1. Coefficients c_k and d_k used in generating the density transfer function in eq. (4).

i	j	k	c_k	d_k
0	0	0	0.14752	0.04329
1	0	1	28.01724	8.26919
1	1	2	−22.70128	−6.65470
2	0	3	19.81050	10.20980
2	1	4	35.61776	14.91155
2	2	5	11.37035	6.29335

Note. In practice, fractional slowness is used as a variable rather than wave speeds. The fractional P-wave slowness $U_{pf} = (1/V_p - 1/V_{pmax})/(1/V_{pmin} - 1/V_{pmax})$, and similarly for the fractional S-wave slowness U_{sf}. Eq. (4) becomes $\rho(U_{pf}, U_{sf}) = \sum_{i=0}^{n}\sum_{j=0}^{i} c_k U_{pf}^{i-j} U_{sf}^{j} / \sum_{i=0}^{q}\sum_{j=0}^{i} d_k U_{pf}^{i-j} U_{sf}^{j}$. We take V_{pmin} and V_{pmax} to be 2.0 and 8.5 km s^{-1}, respectively, V_{smin} and V_{smax} to be 1.0 and 5.0 km s^{-1}, respectively, and $n = q = 2$. The units for U_{pf} and U_{sf} are s km^{-1}.

between $\rho(V_p, V_s(V_p))$ and that resulting from the transfer function. Specifically, for an assumed value of ρ, we calculate $V_p(\rho)$ from the Brocher (2005) relation, and $V_s(V_p)$ from eq. (3). These values for V_p and V_s are substituted into eq. (4) to calculate ρ, and the difference between the calculated and assumed ρ is treated as a residual in a least squares determination of c_k and d_k. A reasonable estimate of a transfer function that meets these requirements (Table 1 and Fig. 7) can be achieved by second order polynomials in both the numerator and denominator (i.e. $n = q = 2$ in eq. 4). Note that for algorithmic reasons, we use fractional slownesses rather than wave speeds as the variables in eq. (4), but the functional form is the same.

4.2 Inverse problem

The inverse problem is based on a standard linear expansion of the combined forward problems. Following a procedure described by Roecker *et al.* (2004, 2006), we solve for perturbations to P slowness ($U_p = 1/V_p$) and the ratio $r = V_p/V_s = U_s/U_p$ rather than to shear wave slowness itself by setting $\Delta U_s = \Delta(rU_p) = U_p\Delta r + r\Delta U_p$. A revised shear wave speed model is then determined from $U_s = rU_p$ after modifying r and U_p with Δr and ΔU_p. This approach allows the S-wave model to take advantage of the nominally greater resolving power of P-waves and also provides a means to couple the sensitivity of U_s determined from the surface waves to perturbations in U_p. It also is advantageous in the interpretation of variations in V_p/V_s as proxies for properties like hydration and melt fraction. We find that determining V_p/V_s by dividing individually determined V_p and V_s can be problematic because of differences in the level of resolution for these quantities.

For body waves, partial derivatives for each observation are calculated along the ray paths. Shear wave observations are included using

$$T_{so} - T_{sc} = \sum_{k=1}^{4} \frac{\partial T_{sc}}{\partial h_k}\Delta h_k + \sum_{i=1}^{m} \frac{\partial T_{sc}}{\partial U_{si}}\left[U_{pi}\Delta r_i + r_i \Delta U_{pi}\right] \quad (5)$$

where T_{so} and T_{sc} are the observed and calculated shear wave traveltimes, respectively. The partial derivatives are taken with respect to h_k, the four hypocentre parameters (latitude, longitude, depth and origin time), and the m values of U_{si} that exhibit sensitivity to the shear wave time (i.e. those that bound the elementary volumes through which the ray passes). Note that while hypocentre coordinates are included as variables in the inversion, they are also relocated in updated models prior to any iteration.

All the body wave analysis discussed here was performed with absolute arrival times, as shown in eq. (5). We also tried including double-differenced arrival times to counter potential effects of coherent noise on our results, but found that the differences in the final model were not significant.

Surface wave phase delay times at a given frequency ω are included in a similar way by relating derivatives of shear wave slowness U_s with respect to phase velocity $c(\omega)$ using the chain rule:

$$T_{so}(\omega) - T_{sc}(\omega) = \sum_{i,j} \frac{\delta T(\omega)}{\delta c_{ij}(\omega)} \sum_{k} \frac{\delta c_{ij}(\omega)}{\delta U_{sijk}} \times \left[U_{pijk}\Delta r_{ijk} + r_{ijk}\Delta U_{pijk}\right], \quad (6)$$

where the indices i, j and k refer to the latitude, longitude and depth coordinates, respectively, of each node in the model.

Gravity is included by specifying the difference between an observed (CBA_o) and calculated (CBA_c) complete Bouguer anomaly as

$$CBA_o - CBA_c = \sum_{i,j,k} \frac{\delta CBA_{ijk}}{\delta \rho_{ijk}} \times \left(\frac{\delta \rho_{ijk}}{\delta U_{p,ijk}}\Delta U_{p,ijk} + \frac{\delta \rho_{ijk}}{\delta U_{s,ijk}}[U_{p,ijk}\Delta r_{ijk} + r_{ijk}\Delta U_{p,ijk}]\right), \quad (7)$$

where $\frac{\delta \rho_{ijk}}{\delta U_{p,ijk}}$ and $\frac{\delta \rho_{ijk}}{\delta U_{s,ijk}}$ are calculated analytically from the transfer function in eq. (4). The derivative $\frac{\delta CBA_{ijk}}{\delta \rho_{ijk}}$ is a form factor calculated as part of the Asgharzdeh *et al.* (2007) method for determining the gravitational attraction of a spherical element.

Each row of the system of linear equations is weighted to compensate for differences in the uncertainties associated with the

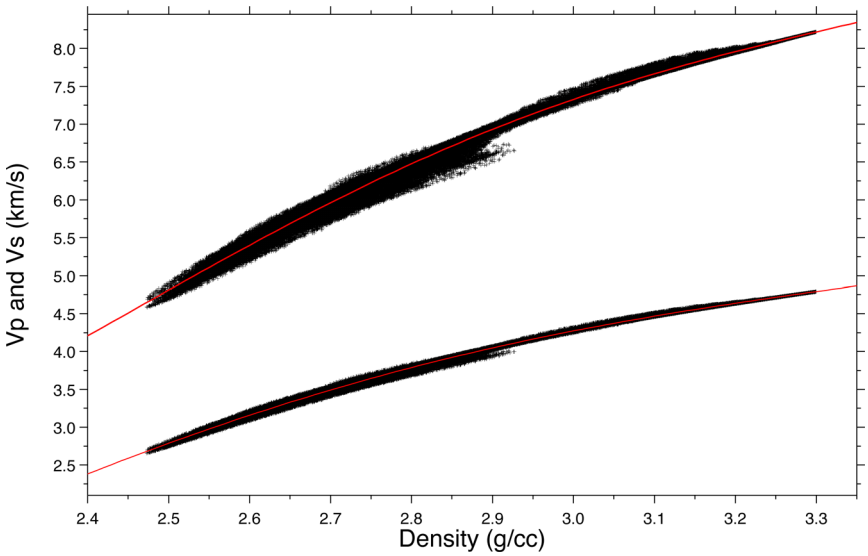

Figure 7. Plot of the density transfer function $\rho(V_p, V_s)$ of eq. (4) used to specify density from values of V_p and V_s. Individual points correspond to $\rho(V_p, V_s)$ for V_p and V_s pairs in the JBS model. Red lines show the transfer function for $V_p(\rho)$ derived from the $\rho(V_p)$ of Brocher (2005) and $V_s(V_p)$ from eq. (3).

corresponding observation. Body wave arrivals are weighted by the inverse of the square of the associated time uncertainty. As mentioned above, data quality criteria are enforced on body wave observations at each iteration to eliminate potential outliers and to disqualify less well constrained hypocentres. Surface wave phase delay times and gravity observations are similarly weighted by their estimated uncertainties. Columnar weighting is applied to compensate for differences in variable units (e.g. km for hypocentres, km s^{-1} for wave speeds, mgals for gravity, and the unitless V_p/V_s ratio) by equalizing the magnitudes of the associated derivatives. In general, for joint inversions we weight the hypocentre, surface wave, and V_p/V_s derivatives by a factor of 10, and gravity derivatives by a factor of 0.1, relative to the wave speed derivatives.

We also applied different strategies for relative weighting of body wave, surface wave, and gravity observations in joint inversions. However, we found from comparison of results with real data that the best result was obtained by first inverting the surface wave phase delay times alone for several iterations prior to jointly inverting both the body and surface waves with even weighting. This step, to some extent, mitigates effects of nonlinearity and compensates both the greater sensitivity of surface waves to shallow structure and the much larger number of body wave observations. The body wave/surface wave model is then used as a starting model for the joint seismic/gravity inversion.

All systems of linear equations are solved iteratively using the LSQR algorithm of Paige & Saunders (1982). In addition to regularization by damping, perturbations to the V_p and V_s models are smoothed after each iteration by averaging neighbouring nodes with a moving window. Based on trial-and-error tests of trade-off between variance reduction and model complexity, we decided to use a window with seven nodes (±3 nodes or ±∼6 km from the centre) in the horizontal directions and 5 nodes (±2 nodes or ±∼4 km from the centre) in depth. Note that as we are smoothing perturbations to the model as opposed to the model itself, smaller scale variations in wave speed still can manifest themselves over several iterations. The ability of this combined data set to recover smaller scale features is demonstrated by the checkerboard and specific structure tests discussed below.

The presented models shown here generally have gone through about 4 iterations with only surface wave observations followed by an additional 10 iterations with combined surface and body wave observations, and finally an additional 10 iterations of combined body wave, surface wave, and gravity observations. Generally, no significant changes in either variance or in wave speeds are realized beyond these last 10 iterations.

4.3 Application

As described above, while all data sets are eventually inverted jointly, we create intermediate models in a step-wise or 'progressive' fashion. Following the example of Comte *et al*. (2016), we allow the surface wave phase delay times to recover a shallow shear wave speed model before including body wave arrival times, and following Roecker *et al*. (2006) we attempt to fit the seismic data before adding gravity observations.

The bounds of the phase velocity maps (1.1 °S–3.4 °S and 35.2 °E–38.0 °E; Fig. 5) were chosen so that Rayleigh waves from GEOFON stations KIBK and KMBO in Kenya could be included. While useful, these stations are well outside the aperture of the CRAFTI-CoLiBrEA network, and the resulting lack of crossing ray paths means that they do not add much more information beyond a first-order estimate of higher V_s wave speeds in the crust to the east of the rift zone. For this reason, we limit the bounds of the model used in the inversion to 1.7 °S–3.4 °S and 35.2 °E–36.8 °E, which encompasses the CRAFTI-CoLiBrEA network. Following Nunn *et al*. (2014), we can still use the phase delays from stations KIBK and KMBO by generating virtual stations along the model boundaries at 36.8 °E and 1.7 °S and calculating phase delays from the CRAFTI-CoLiBrEA stations to these points. These 'virtual' phase delays then act as observed phase delay times along these paths in the inversion, so that, in effect, the phase velocities outside the model are fixed.

We start by deriving a surface wave only (SWO) 3-D model of V_s by inverting phase delay times from the phase velocity maps, corrected for noise-directional bias (Fig. 5). The initial model is

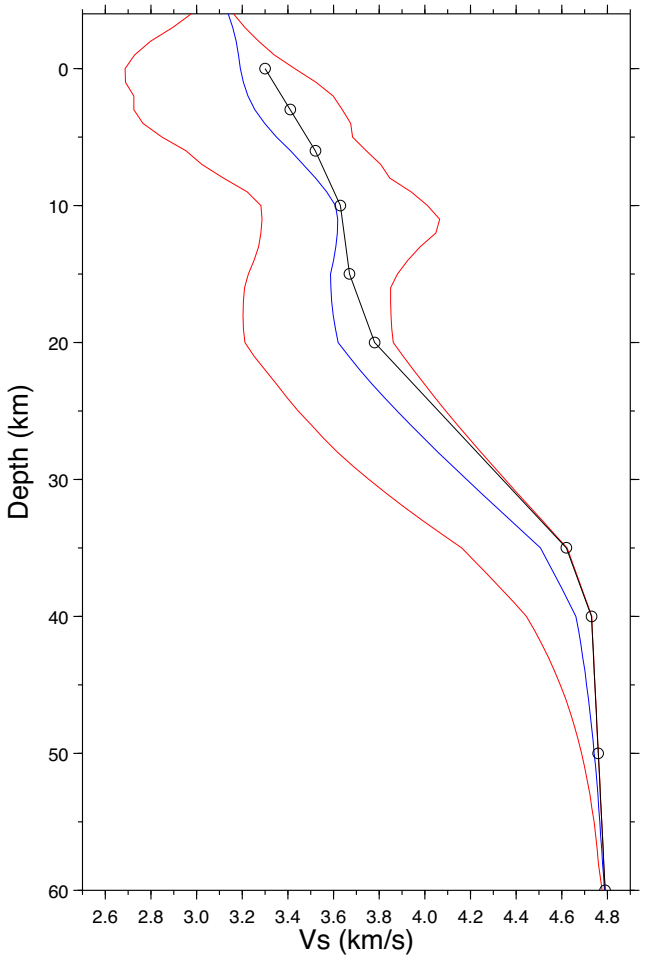

Figure 8. Comparison of the 1-D models of shear wave speed (V_s). Black line with open circles is the starting model taken from Albaric *et al*. (2010). The blue line shows the 1-D average of the 3-D surface wave only (SWO) V_s model. Red lines show the maximum and minimum values of V_s at any depth in the 3-D SWO model.

based on the 1-D results from Albaric *et al*. (2010; Fig. 8). After four iterations, the variance in the phase delay times reduces by 93 per cent, from 0.800 to 0.056 s^2, compared to an anticipated data variance of 0.04 s^2. Note that the 1-D average V_s in the final SWO model remains close to the starting model, although there are significant variations about this mean.

Using the results from the SWO inversion (Supporting Information Figs S2 and S3), we then generate a V_p model by multiplying the corresponding V_s by a constant V_p/V_s ratio of 1.716. This ratio is derived from a Wadati plot of the difference between *S* and *P* travel times (T_s–T_p) versus T_s for the entire data set of 7500 T_s–T_p times (Fig. 9). After 10 iterations of a joint inversion of body wave arrival times and surface wave phase delays (JBS), the variance in the body wave arrival time residuals reduces by 44 per cent from 0.080 s^2 to 0.045 s^2, compared to an anticipated data variance of 0.02 s^2. The variance of the phase delay time residuals remained at 0.056 s^2.

In the final stage, we first use the model from the JBS inversion (Supporting Information Figs S4–S9) to generate a density model using the $\rho(V_p, V_s)$ function in eq. (4). The Bouguer anomaly predicted by this model (Fig. 10) is significantly different from the observed, particularly in areas to the east of the rift valley. The final model, achieved after 10 iterations of the joint inversion of body wave, surface wave, and gravity observations (JBSG), improves the

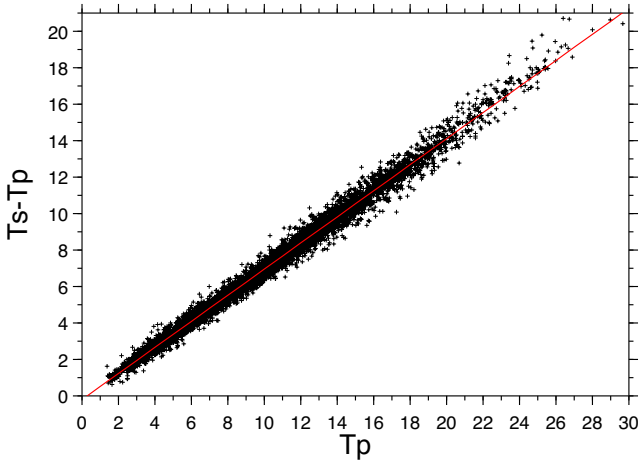

Figure 9. Wadati plot of T_s–T_p versus T_p for the arrival time data set used in this study. The red line corresponds to a V_p/V_s ratio of 1.716 ± 0.001.

RMS misfit to the gravity by 68 per cent from 13.83 to 4.48 mgals (Fig. 10). The final variance of the body and surface waves residuals are slightly lower (0.041 and 0.050 s^2, respectively) than that achieved after the JBS inversion.

5 RESOLUTION AND ROBUSTNESS

To obtain estimates of robustness and resolution for the final JBSG model, we carried out a series of tests, mostly involving inversions of synthetic data in hypothetical models. In each of these tests, the synthetic data reflects the actual phase delay, arrival time, and gravity data available. Calculated values are contaminated with random noise with zero mean and a standard deviation commensurate with uncertainties estimated for the real data. Reconstruction of any hypothetical model follows the same steps as those used in the actual inversion.

5.1 Checkerboard tests

As a standard assessment of resolution, we carried out two checkerboard tests with different sized checkers. The smaller-scale checkers encompass three grid points in each direction (or ∼3 km in depth and ∼6 km laterally), while the larger-scale encompass five grid points in each direction (or ∼5 km in depth and ∼11 km laterally). Note that in both cases, the size of the checker is smaller than the *a posteriori* smoothing window, applied to adjustments at each iteration, of seven lateral and five vertical grid points. The checkers represent ±5 per cent deviations in V_p and V_s from the average background model shown in Fig. 8. The results (Figs 11 and 12) suggest that the smaller-scale checkers are resolvable to depths of about 15 km in the central part of the array, while the larger-scale checkers are resolvable to depths of about 25 km throughout much of the modelled volume. Resolution is best in areas populated by earthquakes, especially for the smaller-scale checkers (Fig. 12). Note that a similar test with ±5 per cent deviations in V_p and V_p/V_s with no variation in V_s (Supporting Information Fig. S10) produced similar results. In addition to providing guidance on the scale of features we can interpret, these tests suggest that body wave arrival times significantly improve the depth resolution of the surface wave only model, and the addition of gravity observations not only allows for the discrimination of some features poorly sampled by seismic waves but also significantly improves the estimate of the amplitudes

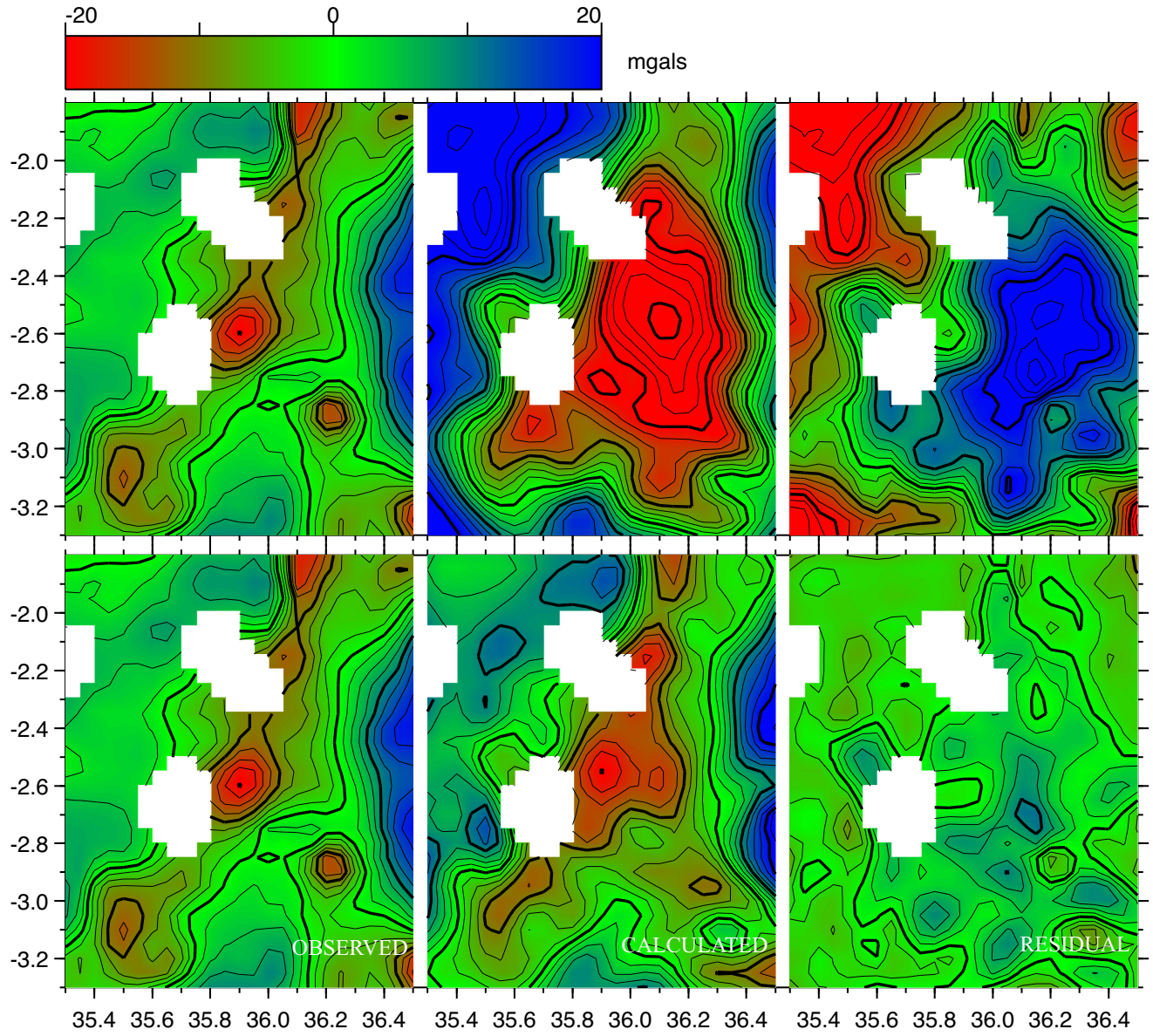

Figure 10. Observed (left), calculated (middle) and residual (right) Bouguer gravity anomalies for the JBS model (upper row) and the JBSG model (lower row). Thin and thick contour intervals are 2.5 and 10 mgals, respectively. White areas have no observations.

of the perturbations, particularly for the smaller-scale perturbations (Supporting Information Figs S11 and S12).

5.2 Reconstruction test

Because checkers generally do not represent actual Earth structure, a reasonable way to test for the existence of modelled features is to see how well the inverse procedure can reconstruct the model itself. Using the final JBSG model as 'truth', we construct a synthetic data set, contaminated by noise at levels assumed to exist in the real data, and repeat the inversion using the same starting model and procedure as that for the real analysis. The point of this exercise is to see if the scale lengths represented in this model are well resolved when flanked by variations in wave speeds suggested by the model, or if, for example, the model might become smoother or smear into undersampled areas. The results of this reconstruction test (Supporting Information Figs S13–S18) show that both the amplitudes and shapes of the prominent anomalies in the model are well recovered. Hence, we conclude that, if the Earth contains anomalies with similar scales and magnitudes such as those represented in the JBSG model, the observations would be able to recover them.

5.3 Tests for specific structures

While checkerboard and recovery tests are necessary to demonstrate model resolution, they do not provide insights into whether specific structures of interest are resolvable. Specifically, and for reasons discussed below, we attempted to recover two closely-spaced bodies with 5 per cent lower wave speeds near the centre of the model at depths between 10 and 25 km. The two bodies are three grid points (∼6 km) wide, seven grid points (∼14 km) long and are separated laterally by an unperturbed three grid point wide region. The results of this test (Supporting Information Figs S19 and S20) demonstrate that if these bodies exist they could be

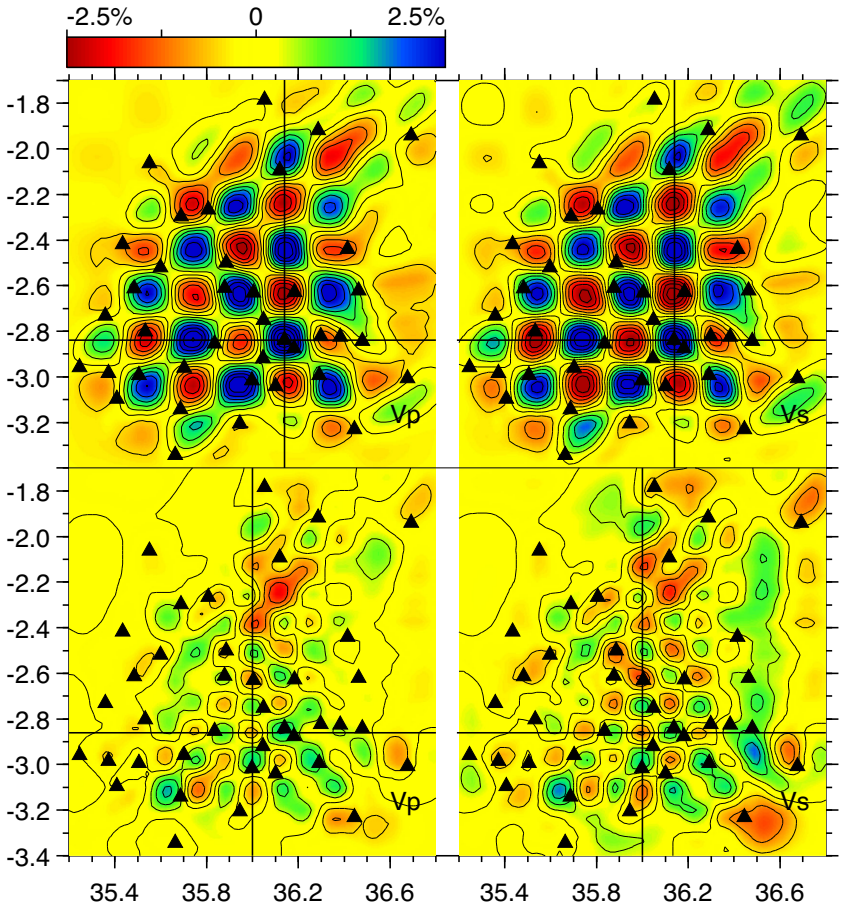

Figure 11. Map views of large-scale (upper row) and small-scale (lower row) checkerboard tests for V_p (left column) and V_s (right column) resolution from the joint body wave, surface wave and gravity (JBSG) inversion model at 13 km depth, plotted as percentage from a null perturbation. Solid black triangles show the CRAFTI-CoLiBrEA seismic network. Bold black lines denote the locations of cross-sections shown in Fig. 12. Contour interval is 0.5 per cent.

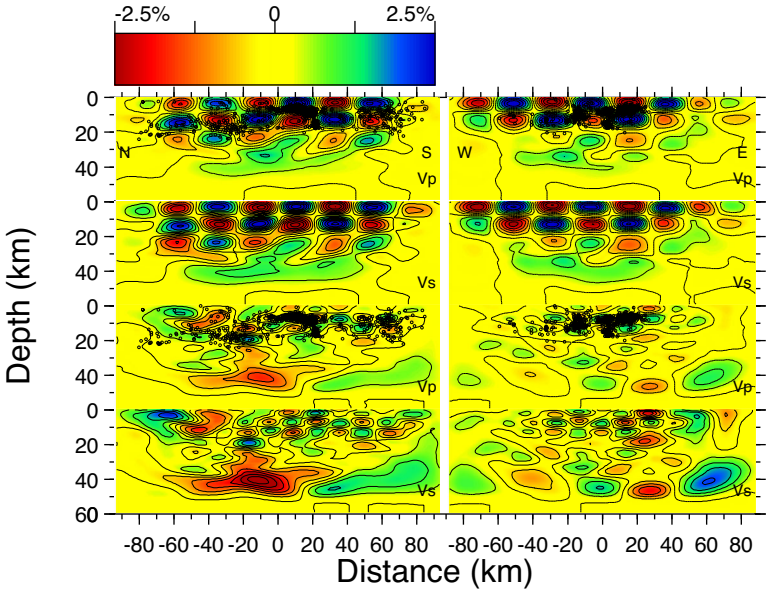

Figure 12. NS (left column) and EW (right column) cross-sections of large-scale (upper two rows) and small-scale (lower two rows) checkerboard tests for resolution of the JBSG inversion, plotted as a percentage from a null perturbation. Locations of cross-sections are shown in Fig. 11. V_p and V_s models are as labelled in the lower right corner of each plot. Contour interval is 0.5 per cent. Earthquakes that occur within ±12 km of the cross-sections are plotted on the V_p results as open circles.

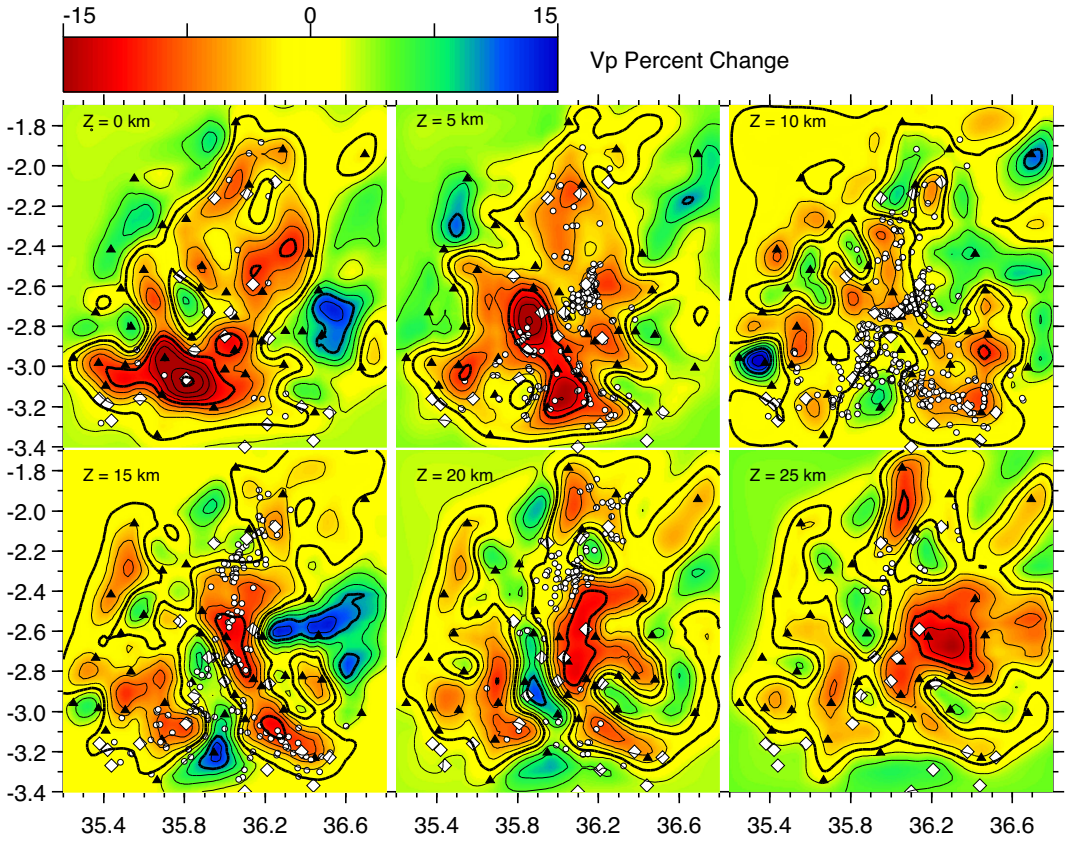

Figure 13. Map views of the JBSG model for V_p at selected depths below mean sea level, as indicated in the upper left corner of each panel. Thin and thick contour intervals are 2.5 per cent and 10 per cent, respectively, from the average at that depth. Black triangles denote the CRAFTI-CoLiBrEA seismic network. Small white circles denote earthquake epicentres. Large white diamonds denote volcanoes.

resolved by the joint inversion. To some extent, this is not surprising since these bodies are larger than the elements that were recovered by the small-scale checkerboard test, but again, it is not obvious that the integrated signal from two larger bodies could be isolated from that due to a smaller intervening body. In particular, we note that, unlike the checkerboard results, these features are not resolved with surface wave observations alone and are only marginally resolved with the combined surface and body wave observations. They are well resolved only by the joint inversion that included both seismic and gravity observations (Supporting Information Figs S19 and S20).

5.4 Sensitivity to starting model

The Albaric *et al*. (2010) results used to generate the starting V_s model for the surface wave inversion has a V_p/V_s ratio of 1.73, slightly larger than the 1.71 value determined from the Wadati plot (Fig. 9). Because of the sensitivity of V_s to partial melt (e.g. Hammond & Humphries 2000), this ratio could seem unusually low for a volcanically active region. Further, in a recent study using similar analysis techniques, Comte *et al*. (2016) determined that their results were more sensitive to relative than absolute values of V_p/V_s. To test our observations for similar sensitivity, we reran the inversion assuming a higher starting V_p/V_s value of 1.78. Reconstructing the Wadati plot with earthquakes located in the Albaric *et al*. (2010) model with this ratio increases the resulting value only slightly to 1.72. Continuing the inverse procedure with a starting value of 1.78 results in a final model that has the same reduced V_p/V_s values as the preferred model. Hence, we conclude that the low V_p/V_s values are robust.

6 DESCRIPTION OF THE JOINT MODEL

To first order, map views (Figs 13–15) and cross-sections (Figs 16–18) of the final model show variations in V_p and V_s that are roughly ±10 per cent from the 1-D average in the upper 25 km. These variations are strongly correlated to one another. For the most part, wave speeds are lower in the rift valley in the central part of the model, particularly in the upper 10 km. Below this depth, the central low bifurcates into an eastern zone underlying the Natron and Manyara rifts and a western zone beneath the Crater Highlands and the Eyasi–Wembere rift. The two zones are separated at about 35.9 °E by a high-wave speed, tabular feature roughly 10 km wide and striking slightly west of north. This high wave speed zone lies beneath the western edge of the Natron and Manyara rifts and is aligned along the bounding fault at the eastern edge of the Crater Highlands horst. Viewed in cross-section (Figs 16 and 17), the low wave speed zone beneath the Natron and Manyara rifts appears to dip to the east, where it underlies the Gelai and Kitumbeine volcanoes.

Despite V_p and V_s being strongly correlated, the V_p/V_s ratio (Figs 15 and 18) varies by as much as ±4.5 per cent from the 1-D average. As mentioned above, the regional average V_p/V_s is low (∼1.71), exceeding 1.78 only in isolated parts of the model. For the most part, V_p/V_s beneath the rift valley is lower than average, ranging from 1.68 to 1.72. However, at depths greater than

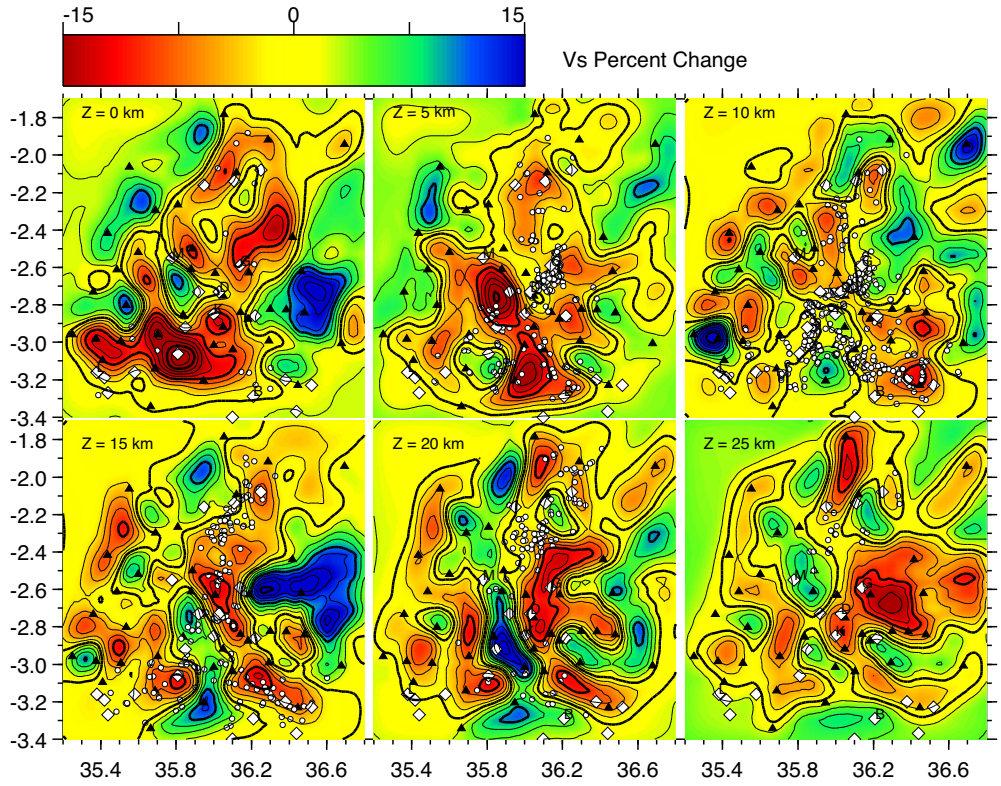

Figure 14. Map views of the JBSG model for V_s at selected depths below mean sea level, as indicated in the upper left corner of each panel. Symbols are the same as in Fig. 13.

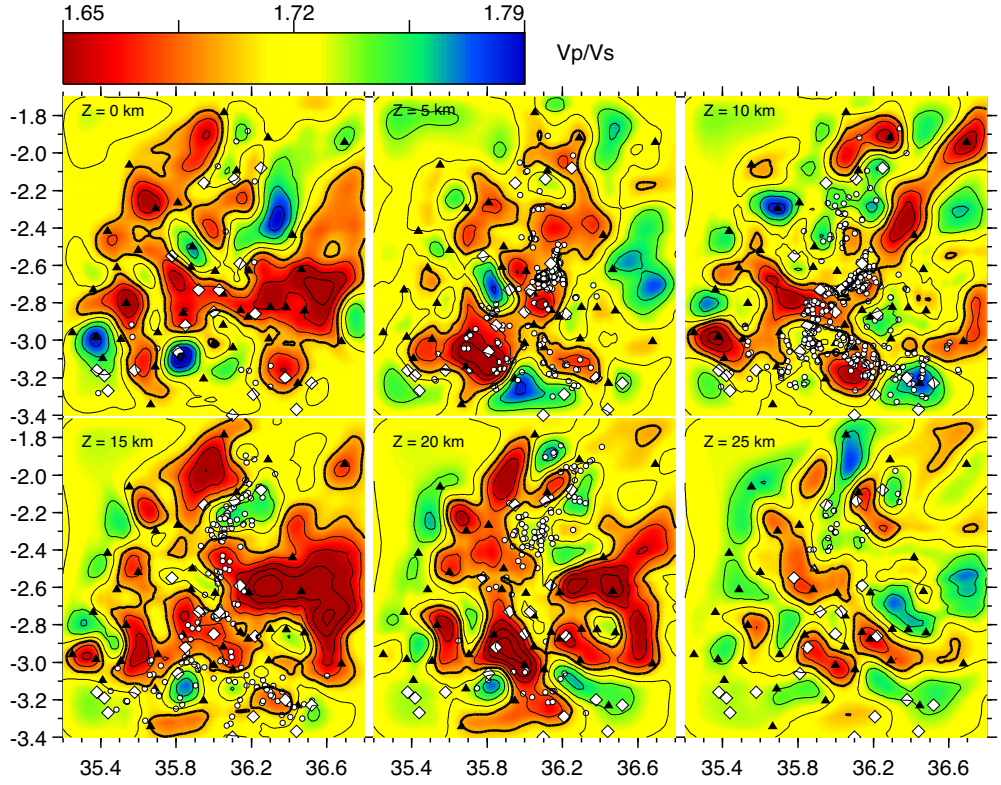

Figure 15. Map views of the JBSG model for V_p/V_s at selected depths below mean sea level, as indicated in the upper left corner of each panel. Thin and thick contour intervals are 0.02 and 0.10, respectively. Symbols are the same as in Fig. 13.

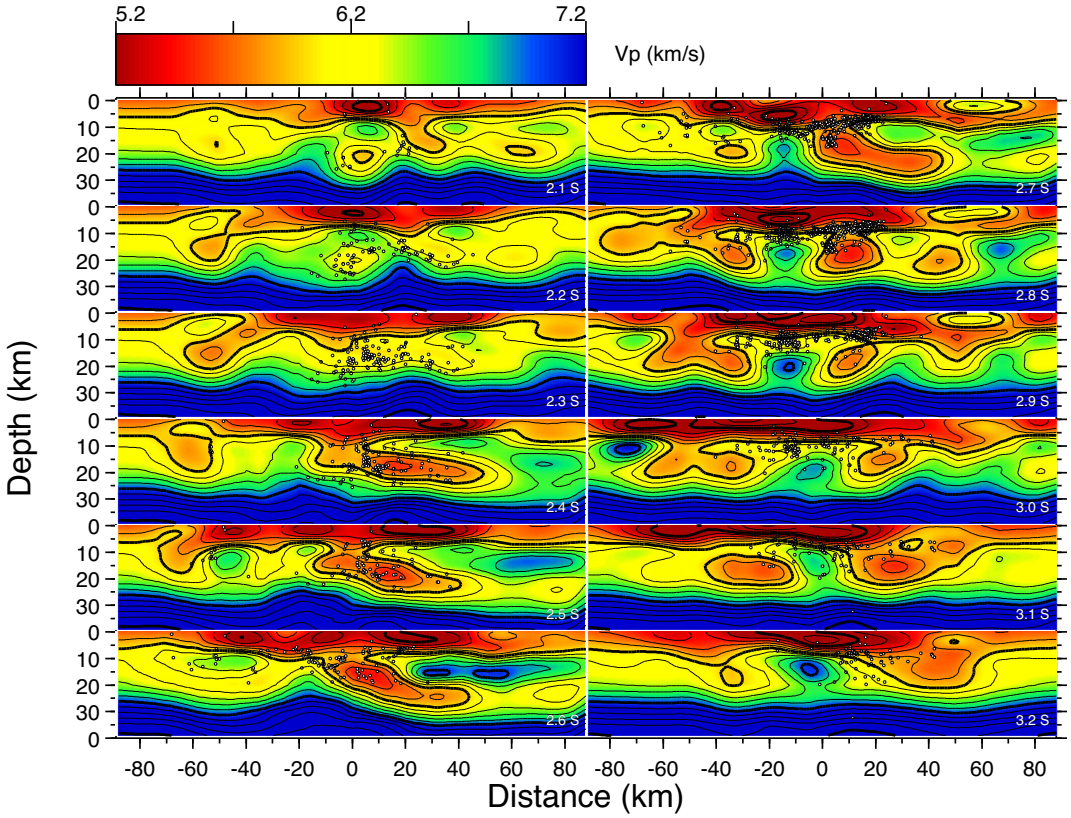

Figure 16. E–W cross-sections of the JBSG model for V_p, taken every 0.1 ° of latitude between 2.1 °S and 3.2 °S. In each section, the left and right sides of the panel are located at 35.2 °E and 36.8 °E and the distance is from the midpoint at 36.0 °E. Thin and thick contour intervals are 0.2 and 1.0 km s^{-1}, respectively, and the thick mid-crustal contour is 6.0 km s^{-1}. Closed white circles denote earthquakes that occur within ±12 km of the section.

about 10 km, the lowest V_p/V_s is more closely associated with the bounding faults on the east and west sides of the valleys. The most coherent, large-scale low V_p/V_s feature runs parallel to the high V_p and V_s tabular region along the western edge of the Natron and Manyara rifts. The other large-scale low V_p/V_s feature is located at depths >10 km below Gelai volcano, again in a region where both V_p and V_s are higher than average. Viewed in cross-section (Figs 16–18), V_p/V_s beneath Galai appears to be inversely correlated with V_p and V_s.

The locations and focal mechanisms of the earthquakes in this region, and their relation to this wave speed model, are discussed in detail in a companion paper (Weinstein *et al*. 2016). To summarize the salient features for this study, we note that the earthquakes used to generate the JBSG model (and relocated in this model) extend from the near surface to ∼20 km depth. They also tend not to occur in regions with higher V_p and V_s, and appear to be most commonly associated with large gradients in wave speed.

7 DISCUSSION

The current best estimates of Moho depth beneath the ERS are from a controlled source experiment across the Magadi basin (Birt *et al*. 1997) and receiver function analysis (Plasman *et al.* 2017) of the CRAFTI-CoLiBrEA data. These estimates range from about 30 to 40 km, with the shallower depths located beneath the rift valley, and straddle the 35 km depth used in the starting model for this study (from Albaric *et al*. 2010). Because our data sets can resolve structure only to depths of 20–25 km, we are imaging only crustal structure. That said, the most significant crustal features recovered in this study are (1) the low *P* and *S* wave speeds underlying almost the entire rift zone, (2) the relatively high wave speed tabular feature located along the western edge of the Natron and Manyara rift zones, and (3) the relatively low V_p/V_s throughout the upper crust, along with the correlations of V_p/V_s with both V_p and V_s in several areas.

A straightforward interpretation of the low V_p and V_s in the upper 4–5 km within the central part of the model is a thick sequence of sediments in the Natron and Magadi rift valleys (Birt *et al*. 1997; Ebinger *et al*. 1997). Based on interpretations of surface deformation patterns (Calais *et al*. 2008; Biggs *et al.* 2009, 2013), one might expect to see some manifestation of the active volcanism that dominates this region at depths below 5 km. Hence the lower V_p and V_s at these depths beneath the rift valleys could be interpreted as a proxy for increased temperatures associated with ascending magma. While the relation of V_p and V_s to temperature depends strongly on lithology (among other variables), a generic estimate of a 0.03–0.08 km s^{-1} decrease in wave speed for a 100 °C increase in temperature (e.g. Christensen 1979; Priestly & McKenzie 2006) would suggest that the observed lateral contrasts in wave speed, on the order of 0.5 km s^{-1}, could represent temperatures elevated by about 1000 °C. This in turn would suggest that temperatures within the mid-crust are high enough for rocks to be molten, particularly when the carbonatite lavas at Oldoinyo Lengai are known to erupt at temperatures as low as 540 °–600 °C (Dawson *et al*. 1994; Pinkerton *et al*. 1995).

In contrast to the low wave speed bodies beneath the central rift, the prominent high wave speed tabular body along the west side of the rift (Figs 13 and 14) most likely does not involve magma.

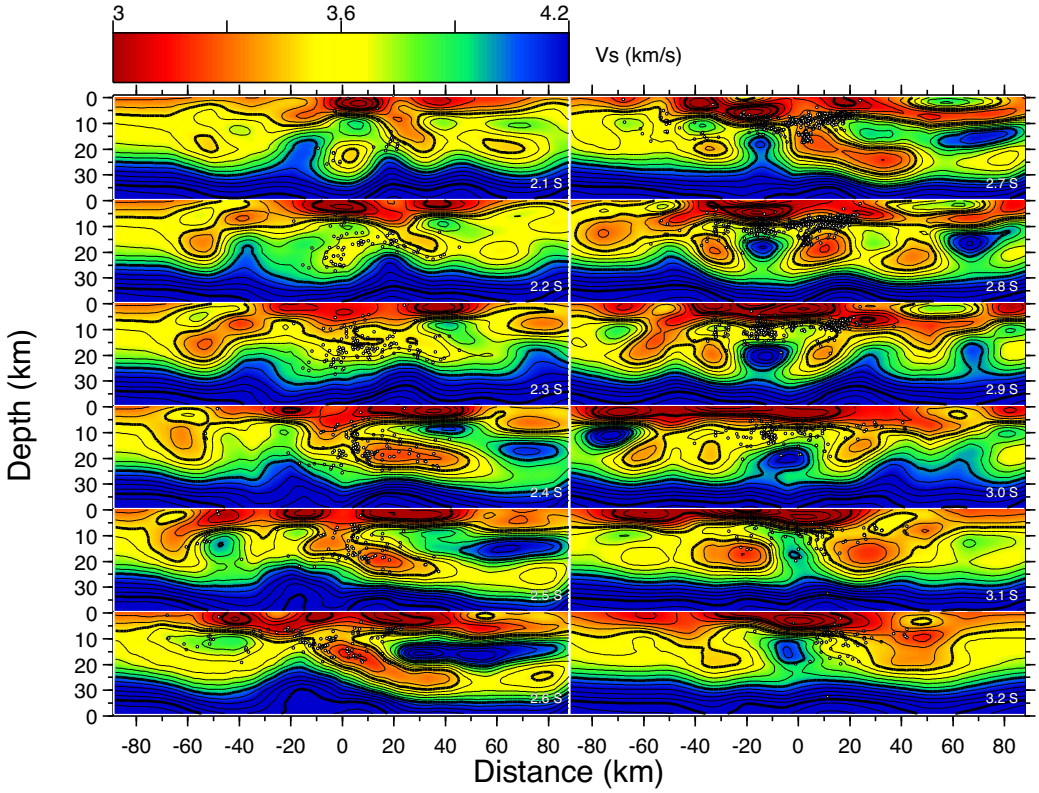

Figure 17. E–W cross-sections of the JBSG model for V_s, taken every 0.1 ° of latitude between 2.1 °S and 3.2 °S. Thin and thick contour intervals are 0.1 and 0.5 km s^{-1}, respectively, and the thick mid-crustal contour is 3.5 km s^{-1}. Symbols are the same as in Fig. 16.

Instead, we interpret the large wave speed gradient on the east side of this feature as the expression at depth of the bounding fault on the west side of the rift, and the high wave speed body as the uplifted and rotated footwall of this normal fault.

While the low V_p and V_s beneath the rift valleys might be due to the presence of partial melt in the mid to upper crust, the sensitivity of V_s to melt typically results in high V_p/V_s ratios for magma chambers beneath active volcanoes (e.g. Greenfield *et al.* 2016). The generally low V_p/V_s ratio determined for this region contrasts with the higher average values found in the crust of the central rift in the Afar region to the north determined by Hammond *et al.* (2011) using H-k analysis of receiver functions. Applying the same type of analysis to the data recorded by the CRAFTI-CoLiBrEA array, Plasman *et al.* (2017) determined significantly higher (1.8–1.9) V_p/V_s for the entire crust beneath the rift valleys, although some stations (KEN4, LN15, LN24, LN26, MW36, PR63) also show a stratification of the crust with lower V_s in the lower crust. Moreover, at one station (KEN4), they determined that V_p/V_s was on the order of 1.73 for the upper 15 km of crust and 1.91 for the lower crust. Combined with our results, this suggests that that V_p/V_s in the upper 15–20 km of the rift valleys is significantly lower than it is in the lower crust and upper mantle. Hence, to the extent that high V_p/V_s reflects the presence of melt, most of that molten rock likely resides in the lower crust and upper mantle rather than the upper part of the crust.

From a lithological point of view, the relatively low V_p/V_s values we determine for the upper crust are not entirely unexpected, as both the natrocarbonatites erupted by Oldonyo Lengai and the trachytes associated with eruptions of Gelai have V_p/V_s ratios on the order of 1.72 (Christensen 1996; Mattsson & Vuorinen 2009), although most of these measurements are done at surface conditions and do not necessary reflect their state in a magma chamber >3 km below the surface. A perhaps more plausible explanation, given what we know about outgassing in the ERS, is that the passageways for magma in the upper crust of the rift valley are water or gas-rich. For example, Lin *et al.* (2014) argue that low V_p/V_s in the seismically active rift zone of Kilauea are likely the result of water filled cracks. Perhaps more appropriate for the ERS, this part of the rift valley is well known for its high volume of CO_2 emissions, particularly near the border faults (Lee *et al.* 2016). Based on theory (Mavko & Mukerji 1995), experiment (Ito *et al.* 1979), and field observations (Julian *et al.* 1995; Harris *et al.* 1996), Julian *et al.* (1998) argue that infiltration of magma-related CO_2 lowered V_p/V_s by about 9 per cent beneath Mammoth Mountain (California). Because V_p/V_s is sensitive to pore-fluid compressibility, largely incompressible magma will be distinguishable from gas phases in pore fluids. Additionally, Parmigiani *et al.* (2016) suggest that large volumes of low density bubbles in the magmatic volatile phase will tend to accumulate at the top of a crystal-rich 'mush' within a magma chamber. As the magma chamber beneath the central part of the rift appears to extend to the bounding faults, these faults would act as a conduit for the outgassing observed at the surface. This could explain not only why V_p/V_s is generally low throughout the model, but also why the lowest values of V_p/V_s in the model are located beneath the normal faults at the edges of the rift valley.

The Natron rift recently (2007–2008) experienced a seismo-volcanic crisis, during which a 2–3 km wide graben, with a cumulative throw of 35–50 cm, appeared on the south flank of Gelai, and a 4 km long, EW-striking dike intruded the eastern flank of Oldoinyo Lengai. Intermittent eruptions of Oldoinyo Lengai during this time transitioned from nephelinitic to carbonatitic lavas. Gelai itself has not erupted in the past 1 My (Mana *et al.* 2015), but a

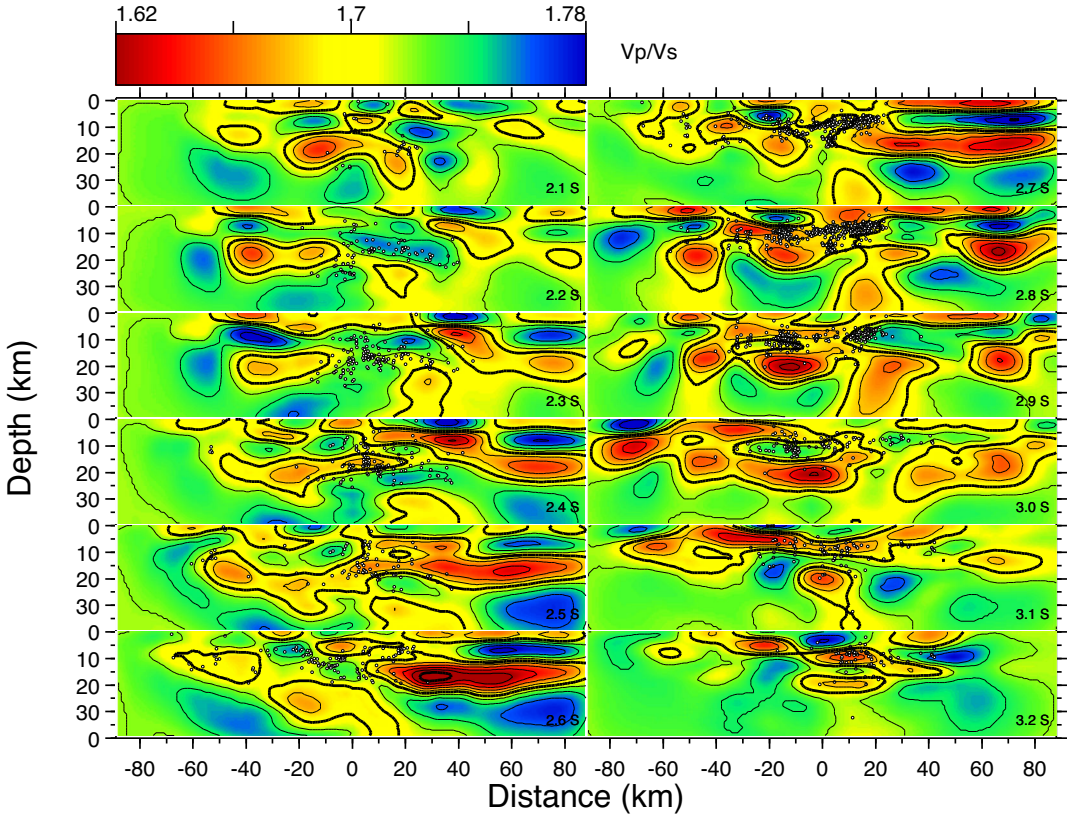

Figure 18. E–W cross-sections of the JBSG model for V_p/V_s, taken every 0.1 ° of latitude between 2.1 °S and 3.2 °S. Thin and thick contour intervals are 0.02 and 0.1, respectively, and the thick mid-crustal contour is 1.70. Symbols are the same as in Fig. 16.

monogenetic cone field of recent melilititic maars and nephelinitic cinder cones appears on its south flank. There is some controversy concerning the plumbing beneath these volcanoes, and whether or not the 2007–2008 activity was the result of multiple, shallow (<5 km depth) magma bodies, as suggested by geodetic models of InSAR data (Calais *et al*. 2008; Biggs *et al.* 2009, 2013). Our model does not reveal multiple chambers beneath the Natron basin, but instead has a singular region of low V_p and V_s in the mid-crust beneath and between the Oldoinyo Lengai and Gelai volcanoes that we would interpret to be a primary storage chamber of magma for these two volcanoes. The test for specific structures discussed previously (section 5.3) suggests that if such features were present, the joint inversion would have resolved them. Our results therefore do not support the interpretation of multiple magma bodies beneath this region, nor of shallow magma storage zones of significant volume. This interpretation is also consistent with receiver functions from piercing points between Gelai and Lengai (Plasman *et al.* 2017).

To summarize (Fig. 19), we suggest that the low V_p and V_s regions in the upper crust beneath the rift valley represent chambers holding magma from the lower crust and upper mantle that is making its way to the surface, but that these chambers themselves are not a long-term repository of molten rock. Rather, they are more likely holding a gaseous 'froth' that contains large amounts of CO_2, and perhaps some water, above a deeper-seated crystal-rich magma mush that occasionally replenishes the shallower chamber prior to eruption. Moreover, this CO_2 appears to infiltrate the surrounding media, substantially lowering V_p/V_s in the regions on the footwall side of the bounding faults, consistent with fault zones as conduits for magma degassing (Lee *et al*. 2016). We do not see any evidence for multiple chambers under the rift valley The lack of any clear compartmentalization of this conduit in the upper crust suggests that the differentiation of magmas that erupt at the surface takes place at greater depths.

ACKNOWLEDGEMENTS

We benefited greatly from the availability of the University of Colorado at Boulder ANCC software package in the Ambient Noise Tomography pre-processing. Special thanks to Mike Ritzwoller for some very helpful insights and advice at critical times of this processing. This research was supported by National Science Foundation grant EAR-1113355 (SR, CE), grant l'Agence Nationale de la Recherche (ANR)- 12-JS06-000401 (CT, JA, SG, SP), and with approval by the Commission for Science and Technology (Tanzania) and the National Council for Science and Technology (Kenya). The seismic instruments were provided by the Incorporated Research Institutions for Seismology (IRIS) through the Portable Array Seismic Studies of the Continental Lithosphere (PASSCAL) Instrument Center at New Mexico Tech. Data collected will be available through the IRIS Data Management Center. The facilities of the IRIS Consortium are supported by the National Science Foundation under Cooperative Agreement EAR-1261681 and the DOE National Nuclear Security Administration. The additional gravity data were collected with a FG5 gravity meter belonging to the national gravity Centre national de la Recherche Scientifique-Institut National des Sciences de l'Univers (CNRS-INSU) facility (https://gmob.resif.fr). We are grateful for logistical support from Tanzania National Parks Commission and to the Ngorongoro National Park. We could not have achieved this work without logistical assistance from primary and secondary school teachers throughout the region, the Maasai

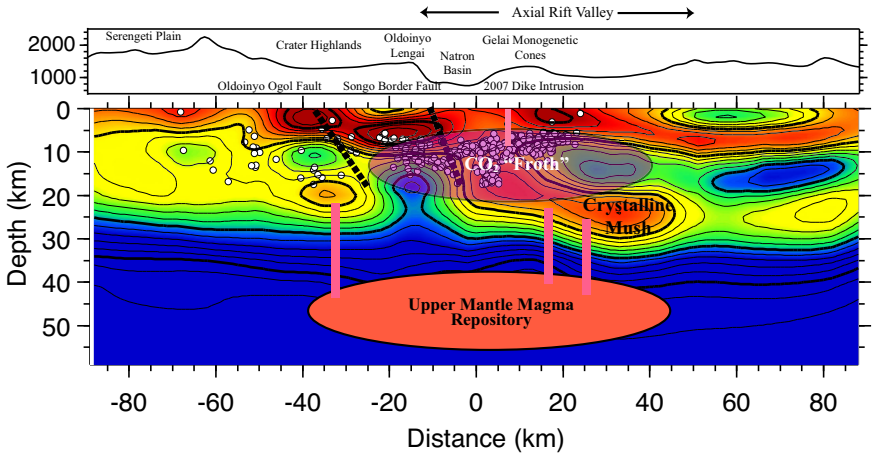

Figure 19. Cartoon summary of the interpretation of the tomographic model. The base image of the lower panel is an EW cross-section of the JBSG model of V_s at 2.7 °S. Distance is relative to 36.0 °E. The colour scale and contours are the same as in Fig. 17. Closed white circles are hypocentres of earthquakes. Thick dashed lines mark the inferred projections of the Songo border fault and the Oldoinyo Ogol fault. Upper panel shows topography along the section (Fig. 1); elevation is in meters. A repository of magma located in the lower crust/upper mantle, and beneath the regions imaged in this study, supplies molten rock to chambers in the mid crust. The magma in the chambers differentiates into a region dominated by a CO_2 froth characterized by low V_p/V_s that permeates a broad region beneath the axial rift valley, above a deeper crystalline mush.

clans in Kenya and Tanzania, and driver-guides from Fortes Tours. This manuscript benefited from the thoughtful comments of Samantha Hansen and an anonymous reviewer.

REFERENCES

Albaric, J. *et al.*, 2010. Contrasted seismogenic and rheological behaviours from shallow and deep earthquake sequences in the North Tanzanian Divergence, East Africa, *J. Afr. Earth Sci.,* **58**(5), 799–811.

Albaric, J., Déverchère, J., Perrot, J., Jakovlev, A. & Deschamps, A., 2014. Deep crustal earthquakes in North Tanzania, East Africa: Interplay between tectonic and magmatic processes in an incipient rift, *Geochem. Geophys. Geosyst.,* **15**(2), 374–394.

Asgharzadeh, M.F., Von Frese, R.R.B., Kim, H.R., Leftwich, T.E. & Kim, J.W., 2007. Spherical prism gravity effects by Gauss–Legendre quadrature integration, *Geophys. J. Int.,* **169,** 1–11.

Ashley, G.M., 2007. Orbital rhythms, monsoons, and playa lake response, Olduvai Basin, equatorial East Africa (ca. 1.85–1.74 Ma), *Geology,* **35**(12), 1091–1094.

Baer, G., Hamiel, Y., Shamir, G. & Nof, R., 2008. Evolution of a magma-driven earthquake swarm and triggering of the nearby Oldoinyo Lengai eruption, as resolved by InSAR, ground observations and elastic modeling, East African Rift, 2007, *Earth planet. Sci. Lett.,* **272**(1), 339–352.

Baptiste, V., Tommasi, A., Vauchez, A., Demouchy, S. & Rudnick, R.L., 2015. Deformation, hydration, and anisotropy of the lithospheric mantle in an active rift: constraints from mantle xenoliths from the North Tanzanian Divergence of the East African Rift, *Tectonophysics,* **639,** 34–55.

Bensen, G., Ritzwoller, M., Barmin, M., Levshin, A., Lin, F., Moschetti, M., Shapiro, N. & Yang, Y., 2007. Processing seismic ambient noise data to obtain reliable broad-band surface wave dispersion measurements, *Geophys. J. Int.,* **169,** 1239–1260.

Bialas, R.W., Buck, W.R. & Qin, R., 2010. How much magma is required to rift a continent?, *Earth planet. Sci. Lett.,* **292**(1–2), 68–78.

Biggs, J., Amelung, F., Gourmelen, N., Dixon, T.H. & Kim, S., 2009. InSAR observations of 2007 Tanzania rifting episode reveal mixed fault and dyke extension in an immature continental rift, *Geophys. J. Int.,* **179,** 549–558.

Biggs, J., Chivers, M. & Hutchinson, M.C., 2013. Surface deformation and stress interactions during the 2007–2010 sequence of earthquake, dyke intrusion and eruption in northern Tanzania, *Geophys. J. Int.,* **195**(1), 16–26.

Birt, C.S., Maguire, P.K.H., Khan, M.A., Thybo, H., Keller, G.R. & Patel, J., 1997. The influence of pre-existing structures on the evolution of the southern Kenya Rift valley—evidence from seismic and gravity studies, *Tectonophysics,* **278**(1), 211–242.

Bott, M.H.P., 1990. Stress distribution and plate boundary force associated with collision mountain ranges, *Tectonophysics,* **182**(3–4), 193–209.

Brocher, T.M., 2005. Empirical relations between elastic wave speeds and density in the Earth's crust, *Bull. seism. Soc. Am.,* **95**(6), 2081–2092.

Buck, W.R., 2004. Consequences of asthenospheric variability on continental rifting, in *Rheology and Deformation of the Lithosphere at Continental Margins*, pp. 1–31, eds Karner, G.D., Taylor, B., Driscoll, N.W. & Kohlstedt, D.L., Columbia Univ. Press.

Calais, E. *et al.*, 2008. Strain accommodation by slow slip and dyking in a youthful continental rift, East Africa, *Nature,* **456**(7223), 783–787.

Chesley, J.T., Rudnick, R.L. & Lee, C.T., 1999. Re-Os systematics of mantle xenoliths from the East African Rift: age, structure, and history of the Tanzanian craton, *Geochim. Cosmochim. Acta,* **63**(7), 1203–1217.

Christensen, N.I., 1979. Compressional wave velocities in rocks at high temperatures and pressures, critical thermal gradients, and crustal low-velocity zones, *J. geophys. Res.,* **84**(B12), 6849–6857.

Christensen, N.I., 1996. Poisson's ratio and crustal seismology, *J. geophys. Res.,* **101,** 3139–3156.

Comte, D., Carrizo, D., Roecker, S., Ortega-Culaciati, F. & Peyrat, S., 2016. Three-dimensional elastic wave speeds in the northern Chile subduction zone: variations in hydration in the supraslab mantle, *Geophys. J. Int.,* **207**(2), 1080–1105.

Dawson, J.B., 1992. Neogene tectonics and volcanicity in the North Tanzania sector of the Gregory Rift Valley: contrasts with the Kenya sector, *Tectonophysics*, **204**(1), 81–92.

Dawson, J.B., Pinkerton, H., Pyle, D.M. & Nyamweru, C., 1994. June 1993 eruption of Oldoinyo Lengai, Tanzania: exceptionally viscous and large carbonatite lava flows and evidence for coexisting silicate and carbonate magmas, *Geology,* **22**(9), 799–802.

Ebinger, C.J., Bechtel, T.D., Forsyth, D.W. & Bowin, C.O., 1989. Effective elastic plate thickness beneath the East African and Afar plateaus and dynamic compensation of the uplifts, *J. geophys. Res.,* **94**(B3), 2883–2901.

Ebinger, C., Poudjom-Djomani, Y., Mbede, E. & Foster, A., 1997. Rifting Archaean lithosphere: the Eyasi-Manyara-Natron rifts, East Africa, *J. Geol. Soc. Lond.,* **154**(6), 947–960.

Ebinger, C. & Sleep, N.H., 1998. Cenozoic magmatism in central and east Africa resulting from impact of one large plume, *Nature,* **395,** 788–791.

Fischer, T.P., Burnard, P., Marty, B., Hilton, D.R., Füri, E., Palhol, F. & Mangasini, F., 2009. Upper-mantle volatile chemistry at Oldoinyo Lengai volcano and the origin of carbonatites, *Nature,* **459**(7243), 77–80.

Foster, A., Ebinger, C., Mbede, E. & Rex, D., 1997. Tectonic development of the northern Tanzanian sector of the East African Rift System, *J. Geol. Soc.,* **154**(4), 689–700.

Foster, A.N. & Jackson, J.A., 1998. Source parameters of large African earthquakes: implications for crustal rheology and regional kinematics, *Geophys. J. Int.,* **134**(2), 422–448.

Gomberg, J.S. & Masters, T.G., 1988. Waveform modelling using locked-mode synthetic and differential seismograms: application to determination of the structure of Mexico, *Geophys. J. Int.,* **94,** 193–218.

Greenfield, T., White, R.S. & Roecker, S., 2016. The magmatic plumbing system of the Askja central volcano, Iceland, as imaged by seismic tomography, *J. geophys. Res.,* **121**(10), 7211–7229.

Hammond, W.C. & Humphreys, E.D., 2000. Upper mantle seismic wave velocity: Effects of realistic partial melt geometries. *J. geophys. Res.,* **105**(B5), 10, 975-10,986.

Hammond, J.O.S., Kendall, J.-M., Stuart, G.W., Keir, D., Ebinger, C., Ayele, A. & Belachew, M., 2011. The nature of the crust beneath the Afar triple junction: evidence from receiver functions, *Geochem. Geophys. Geosyst.,* **12**, Q12004, doi:10.1029/2011GC003738.

Harris, J.M., Langan, R.T., Fasnacht, T., Melton, D., Smith, B., Sinton, J. & Tan, H., 1996. Experimental verification of seismic monitoring of CO_2 injection in carbonate reservoirs, in *SEG Annual Meeting Expanded Technical Program Abstracts with Biographies*, vol. 66, pp. 1870–1872.

Henjes-Kunst, F. & Altherr, R., 1992. Metamorphic petrology of xenoliths from Kenya and northern Tanzania and implications for geotherms and lithospheric structures, *J. Petrol.,* **33**(5), 1125–1156.

Ito, H., DeVilbiss, J. & Nur, A, 1979. Compressional and shear waves in saturated rock during water-steam transition, *J. geophys. Res.,* **84**(B9), 4731–4735.

Jones, A.P., Smith, J.V., Dawson, B. & Hansen, E.C., 1983. Metamorphism, partial melting, and K-metasomatism of garnet-scapolite-kyanite granulite xenoliths from Lashaine, Tanzania, *J. Geol.,* **91,** 143–165.

Julian, B.R., Ross, A., Foulger, G.R. & Evans, J.R, 1995. Three-dimensional seismic image of a geothermal reservoir, The Geysers, California, *Geophys. Res. Lett.,* **23**(6), 685–688.

Julian, B.R., Pitt, A.M. & Foulger, G.R., 1998. Seismic image of a CO_2 reservoir beneath a seismically active volcano, *Geophys. J. Int.,* **133**(1), F7–F10.

Kendall, J.M., Pilidou, S., Keir, D., Bastow, I.D., Stuart, G.W. & Ayele, A., 2006. Mantle upwellings, melt migration and the rifting of Africa: insights from seismic anisotropy, *Geol. Soc. Lond. Spec. Publ.*, **259**(1), 55–72.

Langston, C.A., Brazier, R., Nyblade, A.A. & Owens, T.J., 1998. Local magnitude scale and seismicity rate for Tanzania, East Africa, *Bull. seism. Soc. Am.,* **88**(3), 712–721.

Le Gall, B., Nonnotte, P., Rolet, J., Benoit, M., Guillou, H., Mousseau-Nonnotte, M., Albaric, J. & Deverchère, J., 2008. Rift propagation at craton margin: distribution of faulting and volcanism in the North Tanzanian Divergence (East Africa) during Neogene times, *Tectonophysics,* **448**(1), 1–19.

Lee, H., Muirhead, J., Fischer, T., Ebinger, C., Kattenhorn, S. & Kianji, G., 2016. Tectonic degassing of mantle-derived CO_2 along faults in the East African Rift, *Nat. Geosci.,* **9,** 145–149.

Li, Z., Roecker, S., Wei, B., Wang, H., Schelochkov, G. & Bragin, V., 2009. Tomographic image of the crust and upper mantle beneath the western Tien Shan from the MANAS broadband deployment: possible evidence for lithospheric delamination, *Tectonophysics,* **477**(1–2), 49–57.

Li, Z., Hao, T., Xu, Y. & Xu, Y., 2011. An efficient and adaptive approach for modeling gravity effects in spherical coordinates, *J. Appl. Geophys.,* **73**(3), 221–231.

Lin, G., Shearer, P.M., Matoza, R.S., Okubo, P.G. & Amelung, F., 2014. Three-dimensional seismic velocity structure of Mauna Loa and Kilauea volcanoes in Hawaii from local seismic tomography, *J. geophys. Res.,* **119**(B5), 4377–4392.

Mackwell, S.J., 1998. Hydrogen diffusion and hydrous defect incorporation in mantle olivine, *Terra Abstr.,* **10**(1), 37.

Maggi, A., Jackson, J.A., McKenzie, D. & Priestley, K., 2000. Earthquake focal depths, effective elastic thickness, and the strength of the continental lithosphere, *Geology,* **28**(6), 495–498.

Mana, S., Furman, T., Carr, M.J., Mollel, G.F., Mortlock, R.A., Feigenson, M.D., Turrin, B.D. & Swisher, C.C., III, 2012. Geochronology and geochemistry of the Essimingor volcano: melting of metasomatized lithospheric mantle beneath the North Tanzanian Divergence zone (East African Rift), *Lithos,* **155,** 310–325.

Mana, S., Furman, T., Turrin, B.D., Feigenson, M.D. & Swisher, C.C., 2015. Magmatic activity across the East African North Tanzanian Divergence Zone, *J. Geol. Soc.,* **172,** 368–389.

Mansur, A.T., Manya, S., Timpa, S. & Rudnick, R.L., 2014. Granulite-facies xenoliths in rift basalts of Northern Tanzania: age, composition and origin of Archean lower crust, *J. Petrol.,* **55**(7), 1243–1286.

Mattsson, H.B. & Vuorinen, J., 2009. Emplacement and inflation of natrocarbonatitic lava flows during the March–April 2006 eruption of Oldoinyo Lengai, Tanzania, *Bull. Volcanol.,* **71**(3), 301–311.

Mavko, G. & Mukerji, T., 1995. Seismic pore space compressibility and Gassmann's relation, *Geophysics,* **60**(6), 1743–1749.

Mechie, J., Keller, G.R., Prodehl, C., Gaciri, S.J., Braile, L.W., Mooney, W.D., Gajewski, D.J. & Sandmeier, K.J., 1994. Crustal structure beneath the Kenya Rift from axial profile data, *Tectonophysics,* **236**(1–4), 179–199.

Montagner, J.-P., 1986. Regional three-dimensional structures using long-period surface waves, *Ann. Geophys.,* **4,** 283–291.

Mulibo, G.D. & Nyblade, A.A., 2009. The 1994–1995 Manyara and Kwamtoro earthquake swarms: variation in the depth extent of seismicity in Northern Tanzania, *South Afr. J. Geol.,* **112**(3–4), 387–404.

Nonnotte, P., Guillou, H., Le Gall, B., Benoit, M., Cotten, J. & Scaillet, S., 2008. New K-Ar age determinations of Kilimanjaro Volcano in the north Tanzanian diverging rift, East Africa, *J. Volcanol. Geotherm. Res.,* **173**(1–2), 99–112.

Nunn, C., Roecker, S., Priestly, K., Liang, X. & Gilligan, A., 2014. Joint inversion of surface waves and teleseismic bodywaves across the Tibetan collision zone: the fate of subducted Indian lithosphere, *Geophys. J. Int.,* **198,** 1526–1542.

Nyblade, A.A., Pollack, H.N., Jones, D.L., Podmore, F. & Mushayandebvu, M., 1990. Terrestrial heat flow in East and Southern Africa, *J. Geophys. Res.,* **95**(B11), 17 371–17 384.

Nyblade, A.A., Langston, C.A., Last, R.J., Birt, C. & Owens, T.J., 1996. Seismic experiment reveals rifting of craton in Tanzania, *EOS, Trans. Am. geophys. Un.,* **77**(51), 517–521.

Paige, C.C. & Saunders, M.A., 1982. LSQR: an algorithm for sparse linear equations and sparse least squares, *ACM Trans. Math. Softw.,* **8**(1), 43–71.

Parmigiani, A., Faroughi, S., Huber, C., Bachmann, O. & Su, Y, 2016. Bubble accumulation and its role in the evolution of magma reservoirs in the upper crust, *Nature,* **532**(7600), 492–495.

Pérez-Gussinyé, M., Metois, M., Fernández, M., Vergés, J., Fullea, J. & Lowry, A.R., 2009. Effective elastic thickness of Africa and its relationship to other proxies for lithospheric structure and surface tectonics, *Earth planet. Sci. Lett.,* **287**(1), 152–167.

Petit, C. & Ebinger, C., 2000. Flexure and mechanical behavior of cratonic lithosphere: gravity models of the East African and Baikal rifts, *J. geophys. Res.,* **105**(B8), 19 151–19 162.

Pinkerton, H., Norton, G.E., Dawson, J.B. & Pyle, D.M., 1995. Field observations and measurements of the physical properties of Oldoinyo Lengai alkali carbonatite lavas, November 1988, in *Carbonatite Volcanism. Oldoinyo Lengai and the Petrogenesis of Natrocarbonatites*, pp. 23–36, eds Bell, K. & Keller, J., Springer Verlag.

Plasman, M. *et al.*, 2017. Lithospheric low-velocity zones associated with a magmatic segment of the Tanzanian Rift, East Africa, *Geophys. J. Int.,* **210**(1), 465–481.

Priestley, K. & McKenzie, D., 2006. The thermal structure of the lithosphere from shear wave velocities, *Earth planet. Sci. Lett.,* **244**(1–2), 285–301.

Ritsema, J., van Heijst, H.J. & Woodhouse, J.H., 1999. Complex shear wave velocity structure imaged beneath Africa and Iceland, *Science,* **286**(5446), 1925–1928.

Roecker, S., Thurber, C. & McPhee, D., 2004. Joint inversion of gravity and arrival time data from Parkfield: new constraints on structure and hypocenter locations near the SAFOD drill site, *Geophys. Res. Lett.,* **31,** L12S04, doi:10.1029/2003GL019396.

Roecker, S., Thurber, C. & Roberts, K., 2006. Refining the image of the San Andreas Fault near Parkfield, California using a finite difference travel time computation technique, *Tectonophysics,* **426,** 189–205.

Rudnick, R.L., McDonough, W.F. & Chappell, B.W., 1993. Carbonatite metasomatism in the northern Tanzanian mantle: petrographic and geochemical characteristics, *Earth planet. Sci. Lett.,* **114**(4), 463–475.

Saria, E., Calais, E., Altamimi, Z., Willis, P. & Farah, H., 2013. A new velocity field for Africa from combined GPS and DORIS space geodetic solutions: contribution to the definition of the African reference frame (AFREF), *J. geophys. Res.,* **118**(4), 1677–1697.

Sens-Schönfelder, C., 2008. Synchronizing seismic networks with ambient noise, *Geophys. J. Int.,* **174**(3), 966–970.

Simpson, F.L., Haak, V., Khan, M.A., Sakkas, V. & Meju, M., 1997. The KRISP-94 magnetotelluric survey of early 1995, first results, *Tectonophysics,* **278**(1–4), 261–271.

Stamps, D.S., Flesch, L.M., Calais, E. & Ghosh, A., 2014. Current kinematics and dynamics of Africa and the East African Rift system, *J. geophys. Res,* **119**(B6), 5161–5186.

Tarits, P., Plasman, M., Hautot, S., Gama, R., Mtelela, K., Tiberi, C. & the COLIBREA Team, 2014. The study of the continental lithospheric breakup in East Africa: example of the Tanzanian Rift, in *22nd Electromag. Induct. Workshop,* Weimar, 24–30 August.

Tesha, A.L., Nyblade, A.A., Keller, G.R. & Doser, D.I., 1997. Rift localization in suture-thickened crust, evidence from Bouguer gravity anomalies in northeastern Tanzania, East Africa, *Tectonophysics,* **278**(1–4), 315–328.

Tiberi, C., Gautier, S., Albaric, J., Ebinger, C., Déverchère, J., Ferdinand Wambura, R.F. & Muzuka, A. & the CRAFTI-CoLiBrEA Team, 2016. A multidisciplinary project to address the onset of rifting and the interaction between deformation and inherited fabrics, *EGU Meeting* (EGU2016-8846), 17–22 April, Vienna, Austria.

Vauchez, A., Dineur, F. & Rudnick, R., 2005. Microstructure, texture and seismic anisotropy of the lithospheric mantle above a mantle plume: insights from the Labait volcano xenoliths (Tanzania), *Earth planet. Sci. Lett.,* **232**(3), 295–314.

Walker, K.T., Nyblade, A.A., Klemperer, S.L., Bokelmann, G.H.R. & Owens, T.J., 2004. On the relationship between extension and anisotropy, constraints from shear wave splitting across the East African Plateau, *J. geophys. Res.,* **109,** B08302, doi:10.1029/2003JB002866.

Weeraratne, D.S., Forsyth, D.W., Fischer, K.M. & Nyblade, A.A., 2003. Evidence for an upper mantle plume beneath the Tanzanian craton from Rayleigh wave tomography, *J. geophys. Res.,* **108**(B9), 2427, doi:10.1029/2002JB002273.

Weeraratne, D.S., Forsyth, D.W. & Webb, S.C., 2004. The seismic low velocity zone west of the EPR where an off-axis plume may be feeding the ridge, *EOS, Trans. Am. geophys. Un.,* **85**(47), abstract #V33G-05.

Weinstein, A. *et al.*, 2017. Volatile-assisted rifting in East Africa: Seismicity of the Magadi-Natron-Manyara basins, Africa, *Geochem. Geophys. Geosyst.,* in press.

Wheildon, J., Morgan, P., Williamson, K.H., Evans, T.R. & Swanberg, C.A. 1994. Heat flow in the Kenya Rift zone, *Tectonophysics,* **236**(1–4), 131–149.

Yang, Z. & Chen, W.P., 2010. Earthquakes along the East African Rift system: a multiscale, system-wide perspective, *J. geophys. Res.,* **115,** B12309, doi:10.1029/2009JB006779.

Yao, H. & Van der Hilst, R.D., 2009. Analysis of ambient noise energy distribution and phase velocity bias in ambient noise tomography, with application to SE Tibet, *Geophys. J. Int.,* **179**(2), 1113–1132.

Yao, H., Van der Hilst, R.D. & De Hoop, M.V., 2006. Surface-wave array tomography in SE Tibet from ambient seismic noise and two-station analysis. I. Phase velocity maps, *Geophys. J. Int.* **166,** 732–744.

Zhang, H., Roecker, S., Thurber, C.H. & Wang, W., 2012. Seismic imaging of microblocks and weak zones in the crust beneath the southeastern margin of the Tibetan Plateau, in *Earth Sciences*, ed. Dar, I.A., InTech.

SUPPORTING INFORMATION

Supplementary data are available at *GJI* online.

Figure S1. Locations of gravity observations used in this study. Closed red circles denote the ∼200 new gravity observations occupied during this project (Tiberi *et al*. 2016). Closed black circles are from databases compiled by Ebinger *et al*. (1997) and Tesha *et al*. (1997). These observations were resampled on a regularized grid, and corrected for a regional field attributed to dynamic compensation for the East African plateau (Ebinger *et al*. 1989).

Figure S2. Map views of the SWO model for V_s at selected depths below mean sea level, as indicated in the upper left corner of each panel. Thin and thick contour intervals are 2.5 per cent and 10 per cent, respectively, from the average at that depth. Small white circles denote earthquake epicentres. Compare with the V_s model from the JSBG inversion in Fig. 14.

Figure S3. E–W cross-sections of the SWO model for V_s, taken every 0.1 ° of latitude between 2.1 °S and 3.2 °S. In each section, the left and right sides of the panel are located at 35.2 °E and 36.8 °E and the distance is from the midpoint at 36.0 °E. Thin and thick contour intervals are 0.2 and 1.0 km s^{-1}, respectively, and the thick mid-crustal contour is 3.5 km s^{-1}. Closed white circles denote earthquakes that occur within ±12 km of the section. Compare with the JBSG inversion in Fig. 17.

Figure S4. Map views of the JBS model for V_p at selected depths below mean sea level, as indicated in the upper left corner of each panel. Thin and thick contour intervals are 2.5 per cent and 10 per cent, respectively, from the average at that depth. Small white circles denote earthquake epicentres. Compare with the V_s model from the JSBG inversion in Fig. 14.

Figure S5. Map views of the JBS model for V_s at selected depths below mean sea level, as indicated in the upper left corner of each panel. Symbols and abbreviations are the same as in Fig. S4.

Figure S6. Map views of the JBS model for V_p/V_s at selected depths below mean sea level, as indicated in the upper left corner of each panel. Thin and thick contour intervals are 0.02 and 0.10, respectively. Symbols and abbreviations are the same as in Fig. S4.

Figure S7. E–W cross-sections of the JBS model for V_p, taken every 0.1 ° of latitude between 2.1 °S and 3.2 °S. In each section, the left and right sides of the panel are located at 35.2 °E and 36.8 °E and the distance is from the midpoint at 36.0 °E. Thin and thick contour intervals are 0.2 and 1.0 km s^{-1}, respectively, and the thick mid-crustal contour is 6.0 km s^{-1}. Closed white circles denote earthquakes that occur within ± 12 km of the section.

Figure S8. E–W cross-sections of the JBS model for V_s, taken every 0.1 ° of latitude between 2.1 °S and 3.2 °S. Thin and thick contour intervals are 0.1 and 0.5 km s^{-1}, respectively, and the thick mid-crustal contour is 3.5 km s^{-1}. Symbols are the same as in Fig. S7.

Figure S9. E–W cross-sections of the JBS model for V_p/V_s, taken every 0.1 ° of latitude between 2.1 °S and 3.2 °S. Thin and thick contour intervals are 0.02 and 0.1, respectively, and the thick mid-crustal contour is 1.70. Symbols are the same as in Fig. S7.

Figure S10. Map view of large scale checkerboard tests for V_p (left) and V_p/V_s (right) resolution from the joint body wave,

surface wave, and gravity (JBSG) inversion model at 13 km depth, plotted as percentage from a null perturbation. Solid black triangles show the CRAFTI-CoLiBrEA seismic network. Contour interval is 0.5 per cent.

Figure S11. Map views of large scale (upper row) and small scale (lower row) checkerboard tests for V_s for the SWO V_s (left column), JBS V_s (middle column) and JBS V_p (right column) resolution at 13 km depth, plotted as percentage from a null perturbation. Solid black triangles show the CRAFTI-CoLiBrEA seismic network. Contour interval is 0.5 per cent. Compare with the JBSG results in Fig. 11.

Figure S12. EW cross-sections of large scale checkerboard tests for resolution of V_s in the SWO (top), JBS (middle) and JBSG (bottom) inversions, plotted as a percentage from a null perturbation. Locations of cross-sections are the same as those in the EW sections of Fig. 11. Contour interval is 0.5 per cent. Compare with the JBSG inversion in Fig. 12.

Figure S13. Map views of a JBSG reconstruction test for V_p at selected depths below mean sea level, as indicated in the upper left corner of each panel. Thin and thick contour intervals are 2.5 per cent and 10 per cent, respectively, from the average at that depth. Black triangles denote the CRAFTI-CoLiBrEA seismic network. Small white circles denote earthquake epicentres. Large white diamonds denote volcanoes. Identifying abbreviations are the same as in Fig. 1.

Figure S14. Map views of a JBSG reconstruction test for V_s at selected depths below mean sea level, as indicated in the upper left corner of each panel. Symbols and abbreviations are the same as in Fig. S13.

Figure S15. Map views of a JBSG reconstruction test for V_p/V_s at selected depths below mean sea level, as indicated in the upper left corner of each panel. Thin and thick contour intervals are 0.02 and 0.10, respectively. Symbols and abbreviations are the same as in Fig. S13.

Figure S16. E–W cross-sections of the reconstruction of the JBSG model for V_p, taken every 0.1 ° of latitude between 2.1 °S and 3.2 °S. In each section, the left and right sides of the panel are at 35.2 °E and 36.8 °E and the distance is from the midpoint at 36.0 °E. Wave speeds correspond to the colours in the palette at the upper left. Thin and thick contour intervals are 0.2 and 1.0 km s^{-1}, respectively, and the thick mid-crustal contour is 6.0 km s^{-1}. Closed white circles denote earthquakes that occur within ±12 km of the section.

Figure S17. E–W cross-sections of the reconstruction of the JBSG model for V_s, taken every 0.1 ° of latitude between 2.1 °S and 3.2 °S. Thin and thick contour intervals are 0.1 and 0.5 km s^{-1}, respectively, and the thick mid-crustal contour is 3.5 km s^{-1}. Symbols are the same as in Fig. S16.

Figure S18. E–W cross-sections of the reconstruction of the JBSG model for V_p/V_s, taken every 0.1 ° of latitude between 2.1 °S and 3.2 °S. Thin and thick contour intervals are 0.02 and 0.1, respectively, and the thick mid-crustal contour is 1.70. Symbols are the same as in Fig. S16.

Figure S19. Map view of a test to resolve two small, closely spaced, low-wave speed anomalies representing magma chambers at mid-crustal depths beneath the Natron basin. Upper left panel shows the target as two red rectangles with perturbations of −5 per cent relative to the background. For reference, the CRAFTI-CoLiBrEA seismic network is plotted as solid white triangles. Panels on the top row show V_p and V_s recovery for the JBSG inversion. Bottom row shows V_s recovery for the SWO inversions and V_p and V_s recovery for the JBS inversion. In each plot, the contour interval is 0.5 per cent. Note that the targets are not resolved by the SWO or JBS inversions, but are with the JBSG inversion.

Figure S20. EW cross-section view at 2.66 °S of the test shown in Fig. S19 to resolve two small, closely spaced, low-wave-speed chambers at mid-crustal depths beneath the Natron basin. Top panel shows the target as two red rectangles with perturbations of −5 per cent relative to the background. Lower panels show V_p and V_s recovery for the JBSG inversion, V_p and V_s recovery for the JBS inversion, and V_s recovery for the SWO inversion. In each plot, the contour interval is 0.5 per cent.